



Seismological monitoring of magmatic and tectonic earthquakes in the East Eifel Volcanic Field, Germany

Joachim R. R. Ritter · Konun Koushesh ·
Bernd Schmidt · Jan-Phillip Föst · Julian Bühler ·
Martin Hensch · Sarah M. Mader

Received: 2 January 2023 / Accepted: 15 October 2024
© The Author(s) 2024

Abstract In 2013 there were reports on exceptionally deep earthquakes in ca. 40 km depth below the intraplate East Eifel Volcanic Field, Germany. Due to this observation the regional seismological monitoring network was improved to better explore this unusual seismicity. In order to acquire the necessary instruments, financial resources, and man power, a close partnership was initiated between the local state seismological service and academic research institutions. As an outcome the seismological field

experiment called *Deep Eifel Earthquake Project – Tiefe Eifel Erdbeben (DEEP-TEE)* was accomplished which measures high-quality ground motion recordings since 2014. These measurements are used to study deep magmatic processes around the Laacher See Volcano (LSV) which was the site of a paroxysmal eruption just 13,079 years ago. As the *DEEP-TEE* network is located in a region with a high cultural noise and loose sediments, a careful site selection was a major task. Here, the network design is described and its recordings are used to determine 1-D seismic velocity models (v_p , v_s , and v_p / v_s) with station delay times to relocate the seismic events. The models include a priori information from active seismic experiments, especially in the mantle, to overcome resolution problems. The new velocity models allow to (re)locate the local earthquakes with horizontal and vertical uncertainties of ca. 0.5 km and 2.0 km, respectively. A special highlight of *DEEP-TEE* is the frequent observation of deep low-frequency (< 10 Hz) earthquakes whose hypocentres outline an active translithospheric channel, feeding the magmatic-fluid-volatile system underneath the LSV.

Supplementary Information The online version contains supplementary material available at <https://doi.org/10.1007/s10950-024-10257-w>.

J. R. R. Ritter (✉) · K. Koushesh · J.-P. Föst · J. Bühler ·
S. M. Mader
Karlsruhe Institute of Technology, Geophysical Institute,
Hertzstr. 16, 76187 Karlsruhe, Germany
e-mail: joachim.ritter@kit.edu

B. Schmidt
State Seismological Service, Geological Survey
of Rhineland-Palatinate, Emy-Roeder-Straße 5,
55129 Mainz-Hechtsheim, Mainz, Germany

J.-P. Föst
Teaching and Research Area Neotectonics and Natural
Hazards, RWTH Aachen University, Lochnerstr. 4-20,
52056 Aachen, Germany

M. Hensch
State Seismological Service, Regierungspräsidium
Freiburg, Geological Survey of Baden-Württemberg,
Albertstraße 5, 79104 Freiburg, Germany

Keywords Seismic experiment · Volcano
monitoring · Seismic velocity model

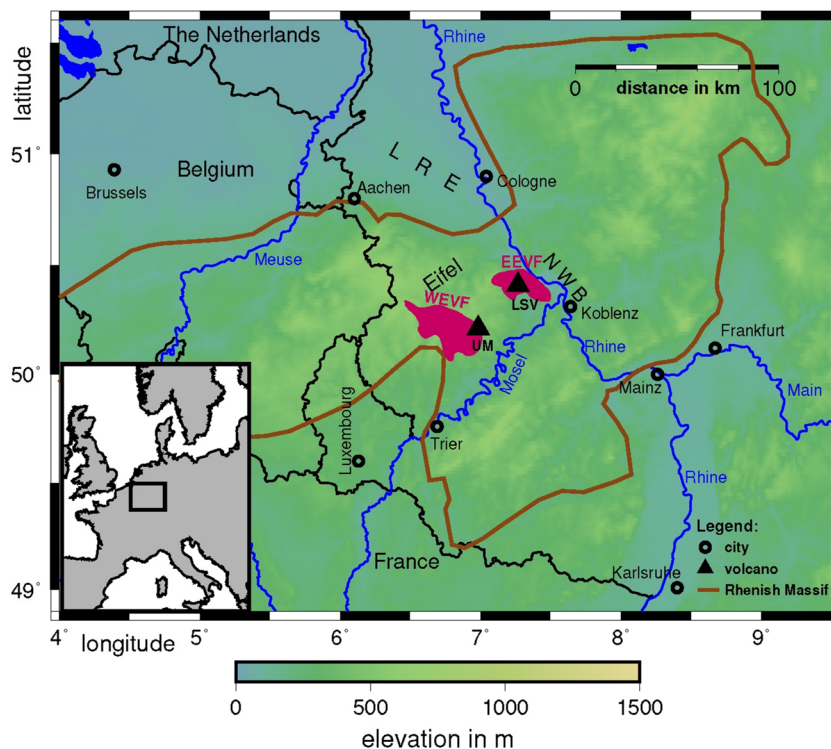
1 Introduction

The monitoring of active and dormant magmatic and volcanic areas is a fundamental task for hazard analyses and research concerning the understanding of magmatic processes (Pallister and McNutt 2015). The parameters gas composition, gas volume flux, ground temperature, gas temperature, ground deformation, seismicity, gravity changes etc. are basic proxies to describe the current situation of magmatic and volcanic processes, as well as to take decisions on hazard alerts (Pallister and McNutt 2015 and references therein). Especially the observation of seismicity, even deeper than the tectonic brittle zone together with source analyses such as fault plane solutions and moment tensor analysis allow us to recover the location and activity rate of the magmatic plumbing system as well as the state of unrest (McNutt et al. 2015; Paulatto et al. 2022). Besides careful operation by the field team, the quality of such recordings depends on the selection of suitable seismic recording sites. In well-developed and densely populated places, seismic recording is strongly influenced by external sources such as seismic noise from man-made activity, e.g., ground motion emissions from traffic or industry

(Trnkoczy et al. 2012). In addition, environmental effects can influence the recording quality: for example, bad coupling of the sensors to the ground due to pyroclastic layers and sediments or a high natural seismic noise level due to water flows, waterfalls, or wind (Bonnefoy-Claudet et al. 2006). Careful planning of a seismological monitoring network needs to minimise such impacts, however, due to given circumstances noise sources cannot always be avoided.

The Eifel is a mountain region in the western part of Germany at the border to Luxembourg and Belgium (Fig. 1). Geologically, it is part of the Rhenish Massif composed of Palaeozoic metamorphic rocks (Meyer 2013). The Eifel was strongly uplifted during the Quaternary (Meyer and Stets 2007; Demoulin and Hallot 2009), a process which is still ongoing and unique in Central Europe (Kreemer et al. 2020). Since ca. 700 kyrs the East and West Eifel Volcanic Fields have been active with together ca. 350 eruption sites (Schmincke 2007). In the West Eifel Volcanic Field (WEVF), the last major activity period started about 80 kyrs ago in the SE part (Mertz et al. 2015) and the last eruption occurred at the Ulmener Maar (UM) just ca. 10.900 yrs ago, leaving behind a 400 m wide crater. In the East Eifel Volcanic Field (EEVF) there

Fig. 1 Map of the study region and surroundings. The brown line outlines the Rhenish Massif; WEVF: West Eifel Volcanic Field, EEVF: East Eifel Volcanic Field, UM: Ulmener Maar, LSV: Laacher See Volcano, NWB: Neuwied Basin, LRE: Lower Rhine Embayment. The inset shows the study region within Europe



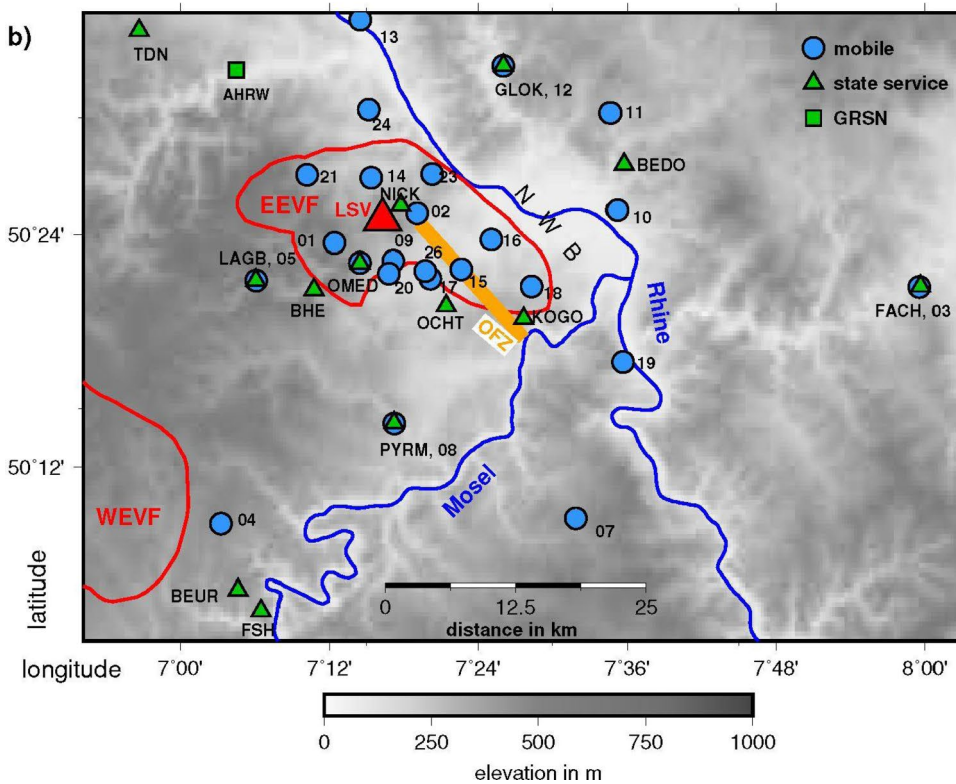
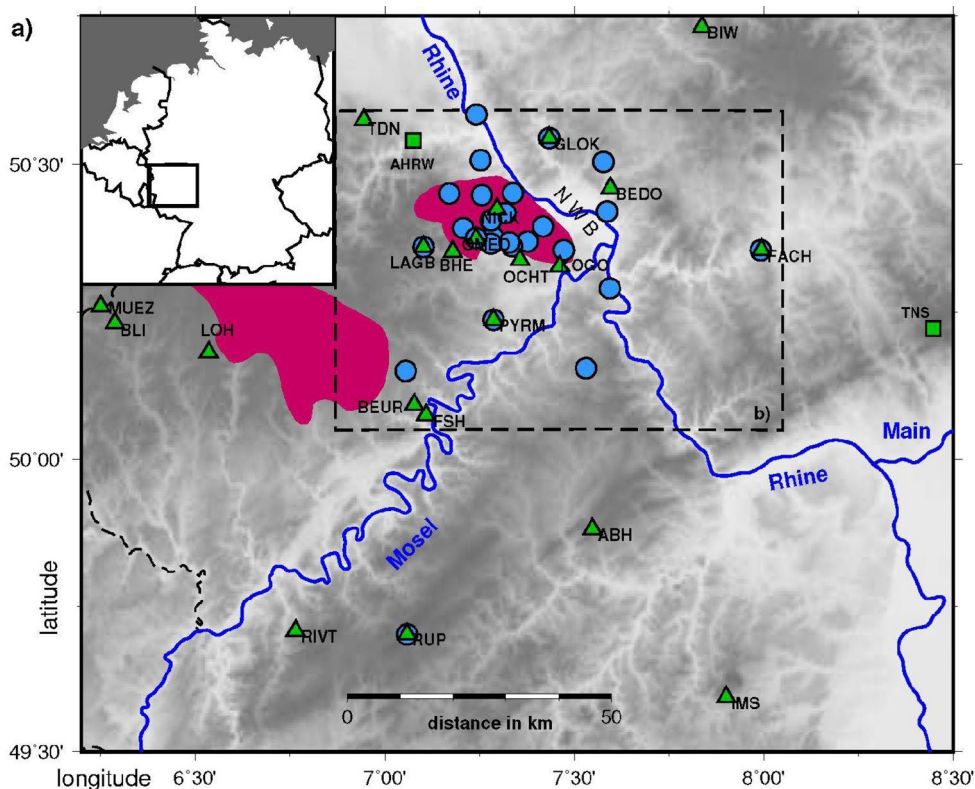
are four major centres. The last eruption occurred at Laacher See Volcano (LSV) as a climactic event of volcanic explosivity index VI about $13,079 \pm 7$ years ago (Reinig et al. 2021). LSV ashes were dispersed over wide regions in Europe and the pyroclastic flows even dammed the river Rhine causing major flooding (Park and Schmincke 2020). Today, a similar ash fall event would cause severe damage to infrastructure (Leder et al. 2017) and a closure of air traffic in Central Europe. Petrological data indicate that the upper crustal magma reservoir of LSV had grown for some 10,000 years (Rout and Wörner 2018) before the last eruption. Based on zircon analyses Schmitt et al. (2022) recently determined 63 ka as possible onset of the presence of evolved magma at the top of the crustal magma reservoir. Nowadays gas emissions (Goepel et al. 2015) and deep seismicity (Hensch et al. 2019) indicate that the volcanic activity is in a dormant state. Based on a comprehensive study Schreiber and Jentzsch (2021) come to the conclusion that there is a relatively high probability for future volcanic eruptions in the Eifel.

Active-source seismological studies indicate that the crust of the EEVF is ca. 29–31 km thick and is underlain by a low seismic P-wave velocity anomaly which is interpreted as magmatic underplating zone (Mechie et al. 1983; Dahm et al. 2020). Below this zone, the lithosphere-asthenosphere boundary is located at just 45–50 km depth (Mathar et al. 2006; Seiberlich et al. 2013). The ca. 20–30 km thick upwelling of the asthenosphere is most probably related to a deep reaching mantle plume as found from teleseismic P- and S-wave tomography modelling (Ritter et al. 2001; Keyser et al. 2002). A buoyant mantle plume can also explain the regional uplift, which is the most significant one in Central Europe north of the Alpine orogen (Kreemer et al. 2020; Cloetingh et al. 2022).

Local seismicity in the Eifel mountains, including the WEVF and EEVF, is quite low (Hinzen 2003; Weber 2012; Hinzen et al. 2021). Known moderate or damaging earthquakes are related to the rifting processes of the Lower Rhine Embayment about 25 km north of the volcanic fields. Especially in the WEVF, earthquake activity is very low with rare swarm-like events (Weber 2012; Hinzen et al. 2021). Seismicity in the EEVF is more frequent but it is below an intensity related to damage (Leydecker 2011). The most active seismic fault is the Ochtendung Fault Zone

(OFZ) (Fig. 2) with about 1–2 weak events ($ML < 1$) per week and occasionally felt shocks ($ML < 4$) (Ahorner 1983; Hinzen et al. 2021). Just east of the EEVF some seismicity occurs in the Neuwied Basin (Hinzen 2003). Recently, deep low-frequency (DLF) seismic events related to magmatic processes were described (Hensch et al. 2019) which are the main target of our network presented here. These DLF earthquakes have hypocenters as deep as ca. 45 km, meaning that they occur in the mantle. Their corner frequency increases with depth what is interpreted that the low-frequency content is not a filtering effect along the propagation path (Hensch et al. 2019). Tectonic activity below ca. 20 km depth is unlikely, because it is not observed in Central Europe north of the Alps (BGR Kataloge 2023). The strength profile of regional continental lithosphere is similar as the one proposed by Jackson (2002) with a single seismogenic layer. Tectonic activity in the uppermost mantle is unlikely (nor observed), because the temperature reaches ca. 800–900 °C below the Moho (Witt-Eickschen 2007) and the wet lithology of the metasomatized lower lithosphere (Witt-Eickschen et al. 1998) should not support enough strength for brittle behaviour (Brace and Kohlstedt 1980; Jackson 2002). The low frequency and long coda waveforms of the DLF events can be better explained by magmatic processes (Wassermann 2012) and this is a reasonable assumption due to the Quaternary volcanism (Schmincke 2007).

Seismic monitoring in the Eifel region before 2014 was not specifically tuned towards observing the magmatic processes underneath the EEVF (Fig. 2a). Only weak tectonic activity was known and mainly short-period instrumentation was installed to monitor this region. Microseismic observation has been started since 1976 by the Seismological Station Bensberg of Cologne University (Ahorner 1983) and continues until today (Weber 2012; Stammer et al. 2021). Later, the Geological Service of North Rhine-Westphalia installed seismic stations (TDN, BHE and LOH) in the Eifel volcanic fields to monitor mainly the strong seismicity in the Lower Rhine Embayment (Fig. 1) at hard-rock sites (Pelzing 2008). The State Seismological Service of Rhineland-Palatinate (SSS R-P) started operation in 1998 and extended its network since then including a dense monitoring of the EEVF (see Sects. 2 and 3 below). Besides these permanent monitoring networks, mobile station



◀**Fig. 2 a** Station map of the study region and surroundings. The East and West Eifel Volcanic Fields are indicated in red, NWB: Neuwied Basin. Green triangles are permanent recording stations of different state seismological services, green squares are broadband recording stations of the German Regional Seismic Network. Blue circles are mobile recording stations, **b** enhanced view with station codes of mobile stations (DEPXX)

deployments were done for passive seismological research projects: Raikes and Bonjer (1983) operated 63 recording stations between 1978 and 1980 across the Rhenish Massif to determine teleseismic travel time residuals. Ochmann (1988) conducted a local teleseismic tomography study around LSV with 14 temporally recording stations in 1985 and 1986. In the framework of the seismological experiment of the Eifel Plume Project about 150 mobile and 100 permanent stations were operated in 1997–1998 with a main focus on the upper mantle structure (GEOFON 1997–1998; Ritter et al. 2000).

In the following we report on the strategy and goals for upgrading of the seismological recording capabilities in the EEVF. This data is used to better detect local tectonic and DLF events as well as locate these events. To improve existing location procedures we determine new local 1-D seismic velocity models with which we relocate the known hypocentre parameters from routine analysis and include new events. Finally, the distribution of the hypocentres is discussed in the context of the established regional geology and magmatism to support hazard analysis.

2 Monitoring strategy

Our earthquake monitoring in the EEVF has two main goals: first, events with $ML > 1$ should be detected and located in real time by the SSS R-P; second, events with $ML > 0$ below LSV (DLF events) and along the OFZ should be detected and observed with the help of recordings from mobile stations deployed by the involved research institutions. This effort should help to reliably detect tectonic and magmatic earthquakes for hazard assessment. The joint network is called the *Deep Eifel Earthquake Project – Tiefe Eifel Erdbeben (DEEP-TEE)* experiment and is composed of a combination of permanent and mobile seismological recording stations with both, offline and online recording. As the observation of

DLF events with frequencies in the range 2–10 Hz is a major goal, only seismometers with a natural frequency of maximum 1 Hz have been deployed. Most seismometers are broadband (Nanometrics Trillium, Streckeisen STS-2) which also cover the frequency range of teleseismic waves and allow the study of deeper mantle structures. All stations from SSS R-P have real time data transmission, whereas most stations from KIT (Karlsruhe Institute of Technology) and GFZ (German Research Center for Geosciences) are operated without online data transmission to save costs and power (station code DEPXX). In addition, mobile phone coverage for data transmission is missing in some remote places in the EEVF.

The backbone of *DEEP-TEE* is the permanent online network of the SSS R-P which operated two stations (OCHT and LAGB) in the EEVF in 2014. It has been upgraded as part of *DEEP-TEE* since then (Fig. 2) and has FDSN code LE. In addition, two online stations (BHE and TDN) from the state network in North Rhine-Westfalia (FDSN code NH) were used in 2014 as well as online station AHRW from the German Regional Seismic Network (Stammler et al. 2021) with FDSN code GR. Following the deep events in 2013, the KIT and GFZ installed 13 mobile recording stations in summer 2014 (Fig. 2). Ten recording stations were provided from the Geophysical Instrument Pool Potsdam (GIPP at GFZ) for two years and afterwards these were replaced by instruments from the Karlsruhe BroadBand Array (KABBA at KIT). The increase of station numbers with time is illustrated in Fig. 3a for the vicinity of the EEVF. At the beginning there were only three permanent short-period stations and the deployment of 13 mobile DEPXX in summer 2014 increased rapidly the recording capacity including a wider frequency band to better record low-frequency signals. Following the removal of the GIPP instruments in summer 2016, the KABBA instruments filled the gaps and since summer 2019 nearly 30 recording stations are available. The FDSN codes for the mobile deployments are 1P (2014–2016) and 9Q (2017–).

The mobile stations were placed in such a way that gaps in the permanent network were filled and that earthquakes as deep as 50 km could be well located. Therefore, a diameter of nearly 100 km was chosen for the *DEEP-TEE* experiment. Azimuthal gaps were closed to allow a good location of the events

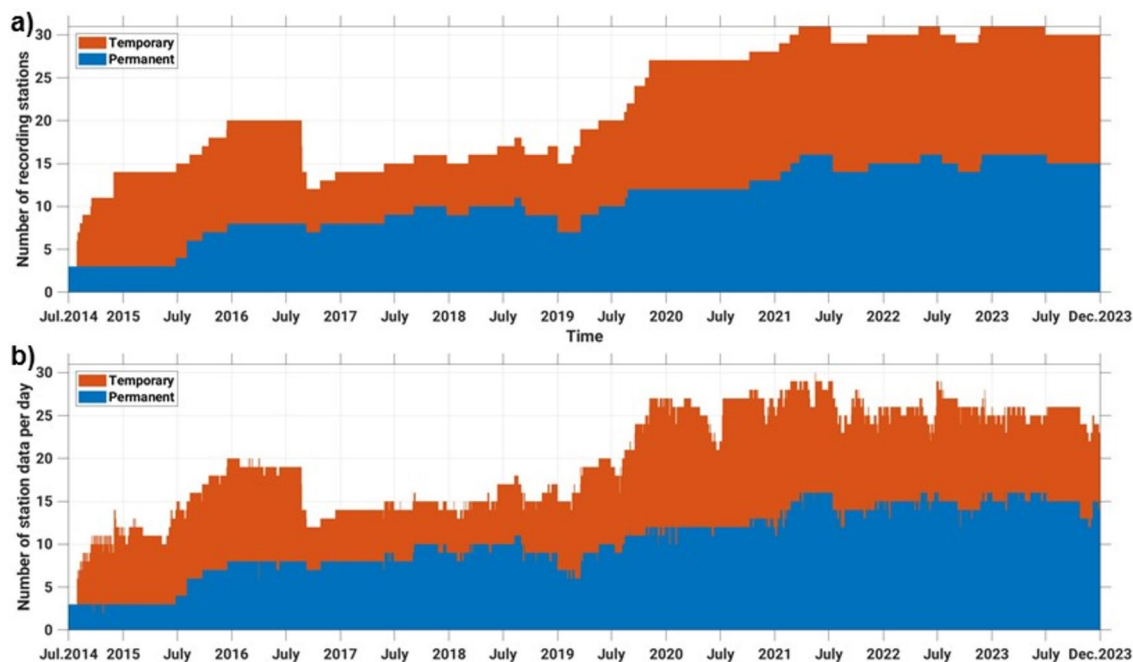


Fig. 3 **a** Station and **b** data availability over time for the DEEP-TEE experiment in the area covered by Fig. 2b. The height of the columns represents the sum of permanent (blue) and mobile (orange) stations (**a**) and the daily station data (**b**)

related to the OFZ (Fig. 2). After the occurrence of upper crustal microseismic swarms north of LSV in 2017, additional mobile stations (DEP21, DEP23 and DEP24) were deployed in the northern part of the network.

After a careful analysis of the first low-frequency events (Hensch et al. 2019) and a comparison with similar recordings from other volcanic regions (Wassermann 2012), it was obvious that this low-frequency seismicity is related to ongoing magmatic processes (see introduction). Then, an upgrade of the permanent SSS R-P network became a high priority since 2015. For this reason, we decided to replace the best mobile station sites with permanent ones. Best in this respect means a low-noise environment and/or a suitable position to improve the determination of rapid real-time event parameters based on automated arrival time readings (Greve et al. 1999). In this way, GLOK replaced DEP12, PRYM replaced DEP08, and OMED replaced DEP22 since 2018 (Fig. 2b). BEDO was installed in the end of 2020 close to DEP10 which was removed afterwards. To enhance the monitoring directly at LSV, a borehole station (NICK) was installed 80 m underneath the surface on the northeast

crater rim of LSV in 2018 to replace DEP02 which was quite noisy. Drilling was necessary to reach solid rock underneath the poorly consolidated volcanic tephra and rocks. In 2020 a mini-array (KOGO) was deployed close to the southern end of the OFZ, consisting of a 3-component central recording station and three surrounding 1-component (vertical) stations. At the end of 2022, within a radius of 40 km from LSV about 28 recording stations contribute to DEEP-TEE for monitoring the EEVF.

3 Station selection criteria and installation

The finding of suitable recording sites is a challenge in the EEVF. In general, its eastern part is a high noise region with dense settlements, traffic, industry, and agriculture in the Neuwied Basin (Fig. 2b). Especially traffic lines are a major problem with two highways (A61 and A49), including large bridges which act as amplifiers for traffic-induced shaking. As the volcanic rocks such as tephra and basalt are widely mined, there are numerous quarries in the region with accompanying blasting activity and heavy traffic. The

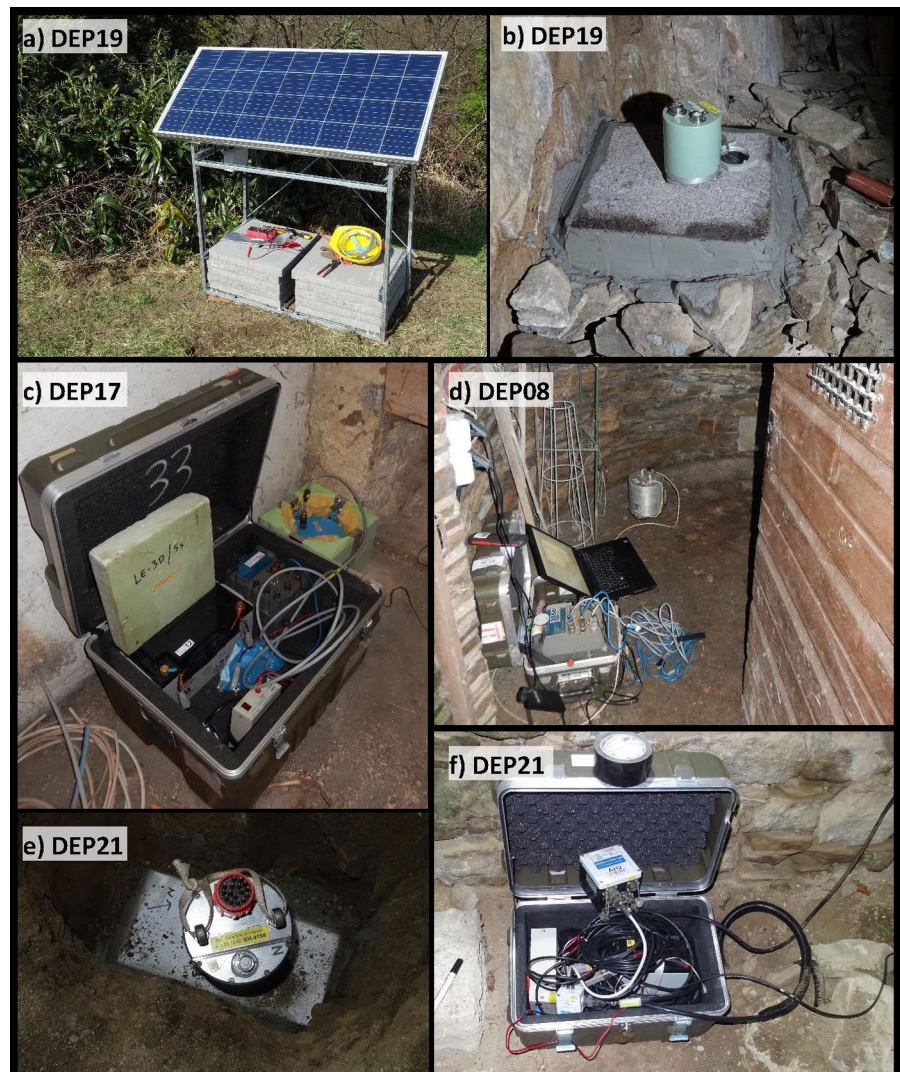
Neuwied Basin just east of the EEVF is filled with Quaternary sediments which amplify the noise from numerous sources: ships on the river Rhine, railway tracks, major roads, and industrial facilities. In its western part, the EEVF is more rural with agricultural land and forests. Here missing infrastructure (power, telecommunication) is an issue at remote low-noise sites. At several places we could not reach basement rock for a good coupling of the seismometer due to the thick pyroclastic layers.

Appropriate recording sites include gun clubs (few activities in evening hours, e.g., DEP16) which are located outside of villages, cemeteries (DEP07 and DEP20), water reservoirs (without pumping activity, DEP01, 02,04,10,11,12,15,18 and 22) or

farms (DEP17 and DEP23). A remote glider airfield (DEP24) also provides a low-noise environment as well as castle ruins (DEP08 and DEP21). Surprisingly, an old 30 m deep, beer cellar (DEP09) in a basalt flow underneath the town of Mendig proved to be a problem for seismic recording: the highway A61 also runs through this basalt flow which carries the strong traffic-induced noise.

Wherever possible, the seismometers are protected against environmental influences by burying them and wrapping them with insulating material (Fig. 4). Since 2020 all seismometers are precisely aligned towards north with a gyrocompass (error $< 0.5^\circ$ during seismometer orientation) what is more accurate than using a magnetic compass.

Fig. 4 Examples of seismic station installations: **a** Solar panel at DEP19, **b** Nanometrics Trillium Compact 120 s sensor on a small concrete pier in a small mine at DEP19, **c** recording equipment (EarthData PR-24 logger with power supply and a Lennartz 5 s seismometer inside a thermal insulation) at DEP17, **d** recording equipment with a MARK 1 s seismometer in the tower of a castle ruin at DEP08, **e** Nanometrics Trillium Compact Posthole 20 s sensor on a small concrete pier in the cellar of a castle ruin at DEP21, **f** recording equipment (CUBE3 with power supply) at DEP21, the sensor (see e) is buried at the right side of the box



Comparisons of magnetic and gyrocompass installations found misalignments reaching 15° for the latter. Flexible plastic tubes are used to protect the GPS antenna cables (Fig. 4) and seismometer cables against rodents. Recently, three sites were equipped with solar panels to reduce battery and travel costs as non-rechargeable batteries with a high capacity of 175 Ah had to be used. However, solar panels are prone to vandalism and can be installed only at safe places. The mobile recording stations without online data transmission are visited every 5–6 months in order to check the equipment and retrieve the data. The data loss due to technical problems is less than 3% (Fig. 3b).

4 Noise analysis and detection thresholds

The seismic background noise is a major issue in the EEVF due to the extensive human activities (see Sect. 3). For quality control of our recordings, we calculate noise spectra using the ObsPy routine PPSD (The ObsPy Development Team 2020). The noise spectra are determined as power spectral densities (PSD_{vel}) of the ground motion velocity calculated for 60 min long time windows. Figure 5 displays PPSD examples.

For comparison with worldwide ground motion recordings, we add the curves of the global New High and New Low Noise Models (NLNM and NHHM) after Peterson (1993). The average noise level PSD_{vel} at the DEEP-TEE sites ranges between the NLNM and the NHHM (Fig. 5). At some sites we find a remarkable difference between a lower noise level at night time and a higher noise level during day time. Such a difference causes a branching of the noise level curves (e.g., DEP14, DEP21, DEP26) in Fig. 5. As consequence of the higher noise level during daytime, we hardly find DLF events between ca. 8 am and 4 pm (local time). In addition, during this time interval also quarry blast activity is high causing similar waveforms as DLF events.

The displayed PSD_{vel} can be used to estimate the approximate resolution threshold of earthquake recordings with regard to the local magnitude ML of events. To relate the amplitude of a signal or earthquake phase with ML we use the standard equation from IASPEI (2013):

$$ML = \log_{10}(A) + 1.11\log_{10}(R) + 0.00189R - 2.09 \quad (1)$$

with A : maximum horizontal displacement amplitude in nm with response function of a standard Wood-Anderson seismometer, and R : hypocentral distance in km. A in Eq. (1) is the maximum shear (S-) wave amplitude ($A_{s_{max}}$) or surface wave amplitude (Alg_{max}) of a local earthquake. As we need a clear recording of the compressional (P-) wave to locate earthquakes, we need to estimate a related P-wave amplitude (A_p) value to rate the sensitivity of a station network. To estimate A_p from A_s we use a relationship of $A_p \sim 0.2 A_s$, because on average actual measurements of local and regional ground motions often have five times larger shear wave amplitudes than compressional wave amplitudes including source radiation and damping effects. Examples for A_p / A_s can be found in Yavuz et al. (2019) or Shelly et al. (2022). In this way P-phases should not be missed. Furthermore, to be able to identify a compressional wave within a noisy background motion, a signal-to-noise ratio of at least 3 is desired. This means a factor of 0.33 is multiplied to A_p to define an approximate maximum amplitude level for acceptable random ground motion displacements (a_{rms}).

We convert expected average a_{rms} values from the observed ground motion velocity PSD_{vel} (Fig. 5) using the equations given in Bormann (1998), e.g.

$$a_{rms} = (PSD_d \cdot f_0)^{1/2} \cdot (2 \cdot (f_u - f_l) / f_0)^{1/2} \quad (2)$$

with f_0 as central frequency of a signal range which has lower and upper frequency limits of f_l and f_u . PSD_d is the power spectral density of the ground displacement (in m^2/Hz) and can be calculated from

$$PSD_d = PSD_{vel} / (4\pi^2 f^2) \quad (3)$$

In an ideal case we would like to determine a DLF earthquake in the upper mantle with $ML=0$ in 50 km hypocentral distance (e.g., 40 km depth and 30 km epicentral distance) which has an amplitude A_s of ca. 1–2 nm. Using a central frequency f_0 of 5 Hz with upper and lower limits of $f_u=9$ Hz and $f_l=1$ Hz for DLF events (Hensch et al. 2019) a maximum noise displacement amplitude a_{rms} of ca 0.1 nm or PSD_{vel} of ca. -180 dB to -185 dB would be desirable for DEEP-TEE sites. Even with low noise conditions during night time this low noise level is hardly fulfilled

Fig. 5 Probabilistic power spectral density of the vertical ground motion velocity at DEEP-TEE sites during summer 2020. The relevant frequency range is between 1 Hz and 20 Hz; here a wider frequency range is plotted as some sensors are broadband (BEUR, DEP01, DEP19, DEP21, NICK). At the time axis, the green line shows data availability (here 100%) and the blue line shows the single PSD measurements that go into the histogram

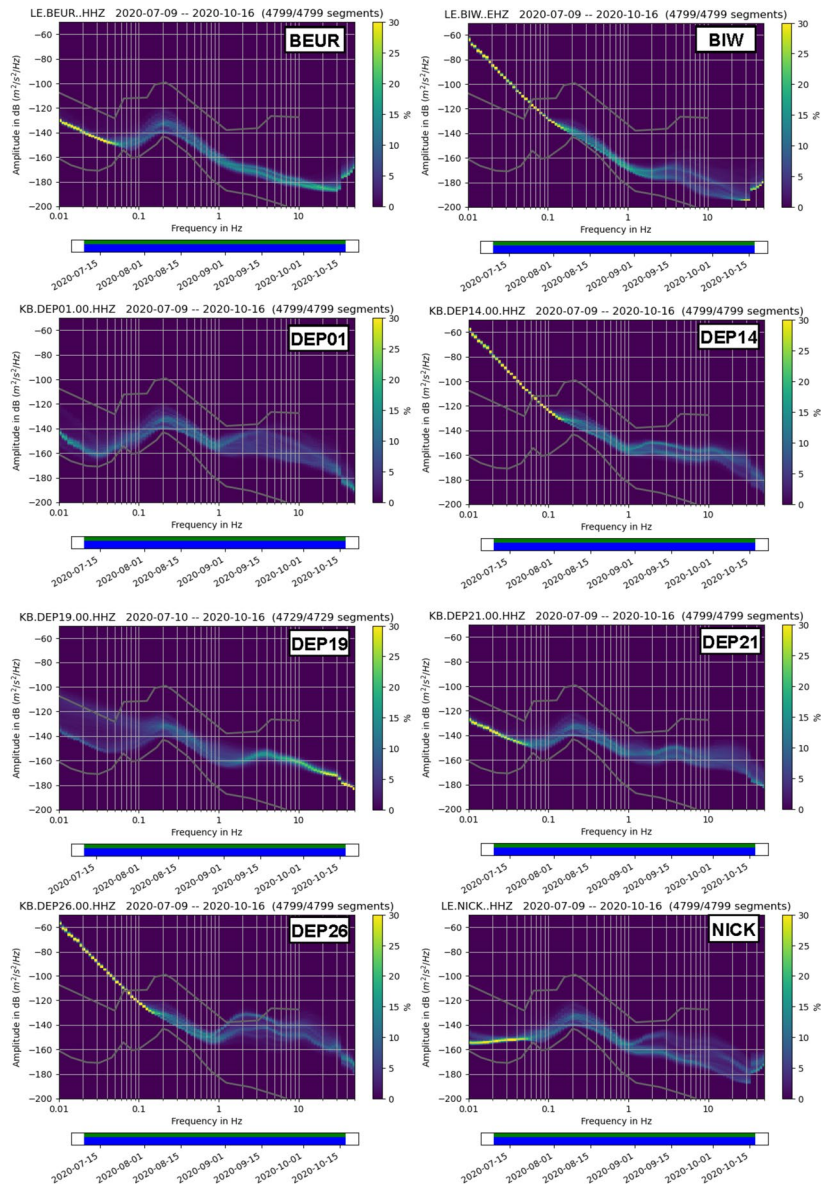


(Fig. 5) and hence we often miss the P-wave of DLF earthquakes, whereas the shear wave trains with higher amplitudes can be observed in many cases.

The PSD_{vel} noise levels between -160 dB and -140 dB at 1–9 Hz, which we find at many DEEP-TEE recording sites in the EEVF, allow us to observe P-wave displacements with $SNR \geq 3$ of ~ 3 nm and ~ 37 nm, respectively. For DLF events at 40 km depth this corresponds to a minimum ML of ~ 1.1 and ML of ~ 2.1 which then can be well located. The quietest recording stations (e.g., DEP04, DEP08 or DEP12 and the permanent

stations) reach -170 dB, especially during night, and then $ML \sim 0$ can be reached. Often the long lasting (10–30 s) shear wave trains of DLF events are identified and earlier tiny signals visible in the noise are estimated as P-wave for location. For this, P-wave characteristics are also investigated using polarisation and component product analyses following Plesinger et al. (1986). Many DLF earthquakes occur at 25–35 km depth and our recording stations directly above these events cannot record clear P-wave signals even at the lower nightly noise levels at ca. -160 dB to -170 dB (Fig. 5).

Concerning shallower tectonic earthquakes related to the OFZ, at ca. 15 km depth and up to 20 km hypocentral distance we take a central frequency f_0 of 15 Hz with upper and lower frequency limits of $f_u = 20$ Hz and $f_l = 10$ Hz (see Hensch et al. 2019). If a P-wave signal with $\text{SNR} \geq 3$ should be recorded, theoretically events with $ML \sim 0.2$ (for -160 dB PSD_{vel}) or $ML \sim 1.2$ (for -140 dB PSD_{vel}) should well be observed with DEEP-TEE data including a very good azimuthal coverage. The actual data analysis reveals that events as weak as $ML \sim 0.3$ are regularly detected and located. The noise level at the broadband stations (see BEUR, DEP01, DEP19, DEP21, and NICK in Fig. 5) is low enough to conduct structural analyses (receiver functions, SKS-splitting etc.) with teleseismic waves.

5 Recording examples

In Fig. 6 we compare waveforms of a DLF event (Fig. 6a) and a tectonic earthquake (Fig. 6b) of similar magnitude ($ML \sim 1$). Both events occurred during night time and they were recorded with a very good signal-to-noise ratio as far as at least 60 km distance at station ABH (Fig. 2a). The DLF event is located at 37 km depth (note the time difference of ca. 5 s between the P- and S-wave close to the epicentre, e.g., at stations OCHT, DEP02 or LAGB). This depth is ca. 7 km below the Moho in the upper mantle. There is a clear difference in the waveforms in Fig. 6: the deep magmatic event emitted low-frequency waves of 1–6 Hz which last for about 15–20 s in the epicentral area. In contrast, the tectonic earthquake radiated high-frequency waves (10–20 Hz) within a short-time rupture process. These characteristics can be used to discriminate the different types of events as well as to automatically identify such signals in the continuous data streams. In Fig. S13 the different components and picked P-wave and S-wave onsets are shown. More examples can be found in Hensch et al. (2019) who also discuss the frequency characteristics of the different earthquake types in more detail.

6 1-D Seismic velocity models (v_p , v_s) and earthquake relocations

The DEEP-TEE recordings of local earthquakes are used to determine local 1-D seismic P-wave velocity (v_p) and S-wave velocity (v_s) models for the EEVF.

These seismic velocity versus depth models are the basis for improved hypocentre parameters from relocations relative to standard locations. As database, we use available pick times from permanent recording stations provided by the SSS R-P (Landeserdbebendienst 2018) and we determine additional onset times of seismic phase arrivals in the time series of the mobile DEEP-TEE recording stations. Especially, newly detected DLF events (Koushesh and Ritter 2024) are carefully picked to include ray paths underneath the tectonic seismogenic zone which reaches down to ca. 17.5 km depth.

As inversion method we apply the VELEST routine (Kissling et al. 1994, 1995) which is stable and well tested. The input parameters for VELEST are the arrival times of the direct seismic P- and S-wave phases, station coordinates, and different starting velocity models. As output, we receive minimum 1-D velocity models, refined hypocentral parameters and individual station delay times for the seismic stations, which take into account local seismic velocity anomalies such as 3-D heterogeneity and anisotropy. In addition, one gets statistical information on the inversion calculation, e.g., the root mean square (RMS) values of the travel time residuals.

6.1 Input data

In total, our event catalogue contains 1762 regional events, which are composed of 1475 events from bulletin files in the years 2010–2021 (Landeserdbebendienst 2018), 319 DLF and 1135 tectonic events in the years 2014–2021 and 155 DLF and 547 tectonic events in the years 2018–2021 when most DEEP-TEE stations were recording (Fig. 3). The velocity model is confined to the region around the EEVF, because we want to concentrate on the DLF events and the seismicity of the OFZ. Therefore, recordings from events are chosen from an area which is restricted to $6.81^\circ\text{E} < \text{longitude} < 8.13^\circ\text{E}$ and $50.0^\circ\text{N} < \text{latitude} < 50.75^\circ\text{N}$. A maximum epicentral distance of ca. 80 km to the centre of the network and a maximum azimuthal observational gap of 180° is allowed; only few events at the borders have a gap of 160° – 180° , mostly it is much less. The event selection criteria reduce the amount of input events for VELEST to 1325 events.

Phase picking of first P- and S-wave arrivals is done manually following the criteria in Diehl

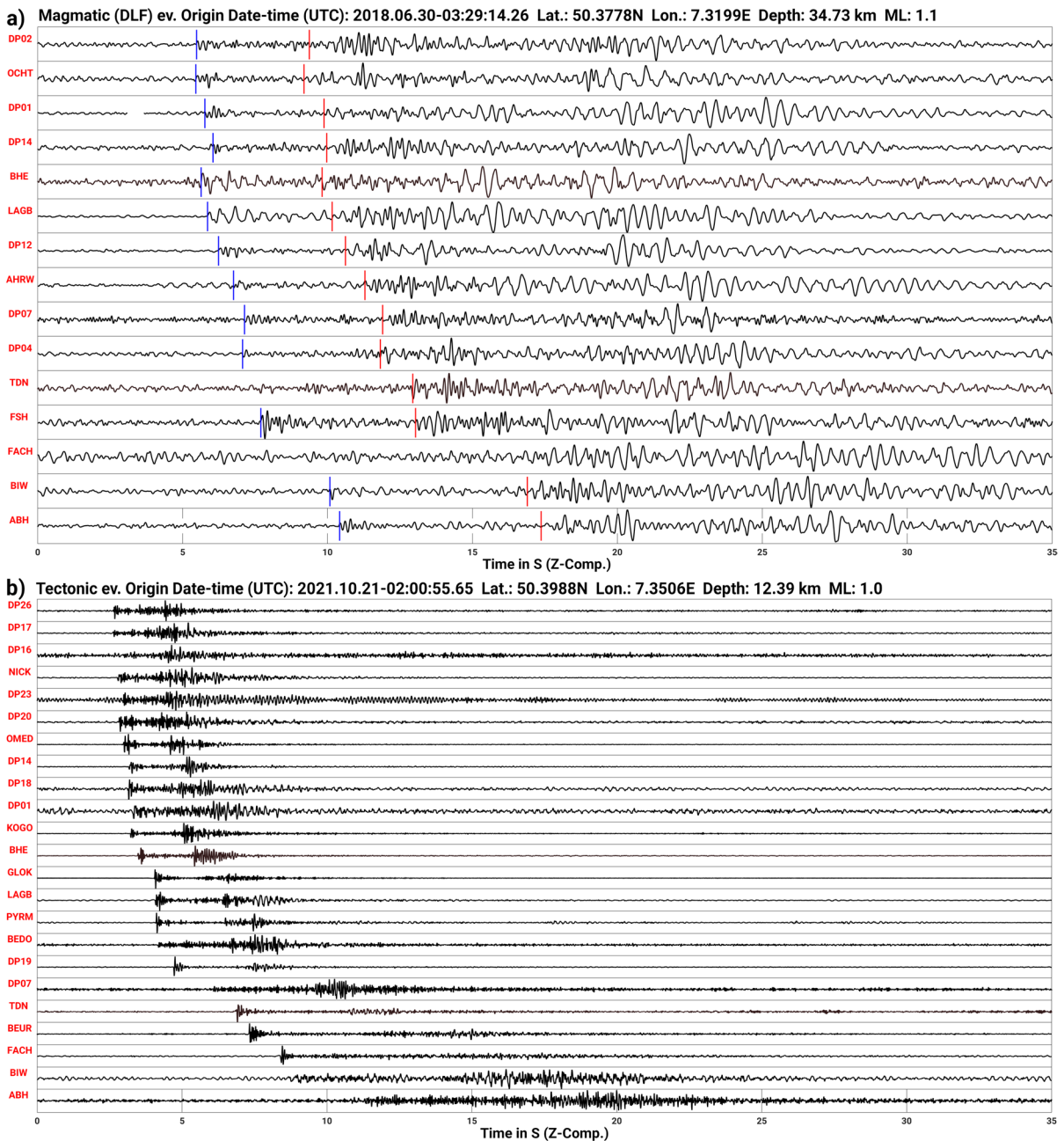


Fig. 6 Recordings of two different types of earthquakes in the East Eifel Volcanic Field, **a** the source is a deep low-frequency event at about 35 km depth with long-lasting waveforms. P-wave (blue) and S-wave onsets (red) are marked, **b** a tectonic event from the Ochtendung Fault Zone at about 12 km depth

with high-frequency waves of short duration. The displayed vertical ground motion amplitudes are trace-normalised and the seismograms are ordered by distance from top to bottom. See Fig. S13 for horizontal component recordings of the DLV event

et al. (2012). To account for different accuracies of the time readings of the phase arrivals, we use a quality weighting scheme. This scheme

is based on the following quality classes: a high quality (quality class 0) means that the maximum uncertainty for the picking time of a phase

is $\Delta t \leq 0.05$ s. A lower quality (quality class 1) is for an uncertainty of $0.05 \text{ s} < \Delta t \leq 0.1$ s. Uncertainties of $0.1 \text{ s} < \Delta t \leq 0.2$ s are rated as quality class 2. Larger uncertainties are rated as quality class 3 ($0.2 \text{ s} < \Delta t \leq 0.4$ s) and quality class 4 ($\Delta t > 0.4$ s) which are both not used for the further analysis steps. After this quality ranking, 2598 P-wave and 3491 S-wave arrival times are available for the inversion (Table S5).

The distributions of the travel time residuals are displayed in Fig. 7 for quality classes 0, 1, and 2, separately for P-wave arrivals (Fig. 7 a-c) and S-wave arrivals (Fig. 7 d-f). The theoretical travel times are calculated with the existing local reference velocity model by Ahorner (1983), see Fig. S1 in the supplement. The distributions in Fig. 7 are close to Gaussian distributions and, as expected from the quality ranking of the picking procedure, the residuals increase from quality class 0 to quality class 2 (the statistical numbers are given in Fig. 7). In general, the residuals are quite small, less than 0.5 s, indicating that the Ahorner model (1983) is one possible appropriate reference or starting model for further inversions with VELEST.

Figure 8 shows the depth distribution of the events from which the arrival times (qualities 0–2) are picked and which we use as three input data sets VI1-V3 (Table S5) for VELEST. VI1 contains P-wave picks with at least 8 picks from 201 events with a hypocentral depth $d < 17.5$ km and at least 6 picks from events with $d > 17.5$ km, altogether 2049 picks. VI2 contains S-wave picks with the same criteria as VI1 for P-waves, altogether 3038 picks from 320 events. VI3 is composed of pick times from 382 events with at least 8 P- or 8 S-wave picks for $d < 17.5$ km and 6 P- or 6 S-wave picks for $d > 17.5$ km (2598 P- and 3491 S-wave picks). Most picked phases are from earthquakes in the upper crustal seismogenic zone (< 17.5 km depth), especially from earthquakes of the OFZ. All deeper phases are from DLF events with more uncertain arrival times due to a lower signal-to-noise ratio and the more emergent DLF waveforms compared to the impulsive waveforms of tectonic ruptures. A special feature in Fig. 8 is the higher number of S-phases relative to P-phases for events below the seismogenic zone; numbers are given in Table S5. Typically, in seismological studies the amount of data from P-phases is higher than the number of

S-phases. However, in our case, the P-phases of the DLF events are often not visible or quite uncertain, whereas the S-wavetrains with higher amplitudes are better visible (see Sect. 4). Hence, v_s is better constrained in the lower layers compared to v_p . This point is described below in more details, because it strongly influences the inversion process.

We use the permanent station OCHT (Fig. 2b) as reference station for our model, because it is close to the centre of the network in the EEVF and it was available from the start of the experiment. Therefore, station OCHT is also one of the stations with most determined phase arrival times.

A Wadati diagram (Fig. 9) is plotted to retrieve the v_p / v_s values as additional a priori information from the dataset. The Wadati diagram indicates a relatively low v_p / v_s which seems to increase with depth: 1.62 for events in the upper crust, 1.68 for events in the lower crust, and 1.68 for events in the uppermost mantle (standard deviations are less than 0.01). These values are averages along the complete ray path from the source to the receiver. Thus, the actual v_p / v_s value may be higher in the deeper layers, as rays from these layers have to traverse the upper crust. The Ahorner model (1983) has a v_p / v_s value of 1.69 in the crust and 1.70 in the uppermost mantle (Table S1); both values are below 1.73, the value for a standard elastic body.

We use three different starting models and perturbations of each of these as input models for VELEST to probe the model space and find an appropriate layering. We use the seismic velocity structures from two previous studies in the region. The Ahorner model (1983), see Fig. S1 and Table S1, was determined using earthquake data from the western Rhenish Massif region. Here the resolution with depth is restricted to the distribution of the earthquake data, which consist of events with a maximum depth of ca. 17.5 km (Ahorner 1983). The model by Mechie et al. (1983), see Fig. S1 and Table S2, is from an active-source seismic-refraction experiment and we take the model part at the EEVF which has a Moho depth of ca. 29 km. This model has a better depth resolution as Ahorner (1983) due to the deep reaching ray paths of the long refraction seismic profile. The third model is a very simple model with one layer in the crust and one layer in the mantle only plus a thin near-surface layer after Eickhoff (2022) (Fig. S3).

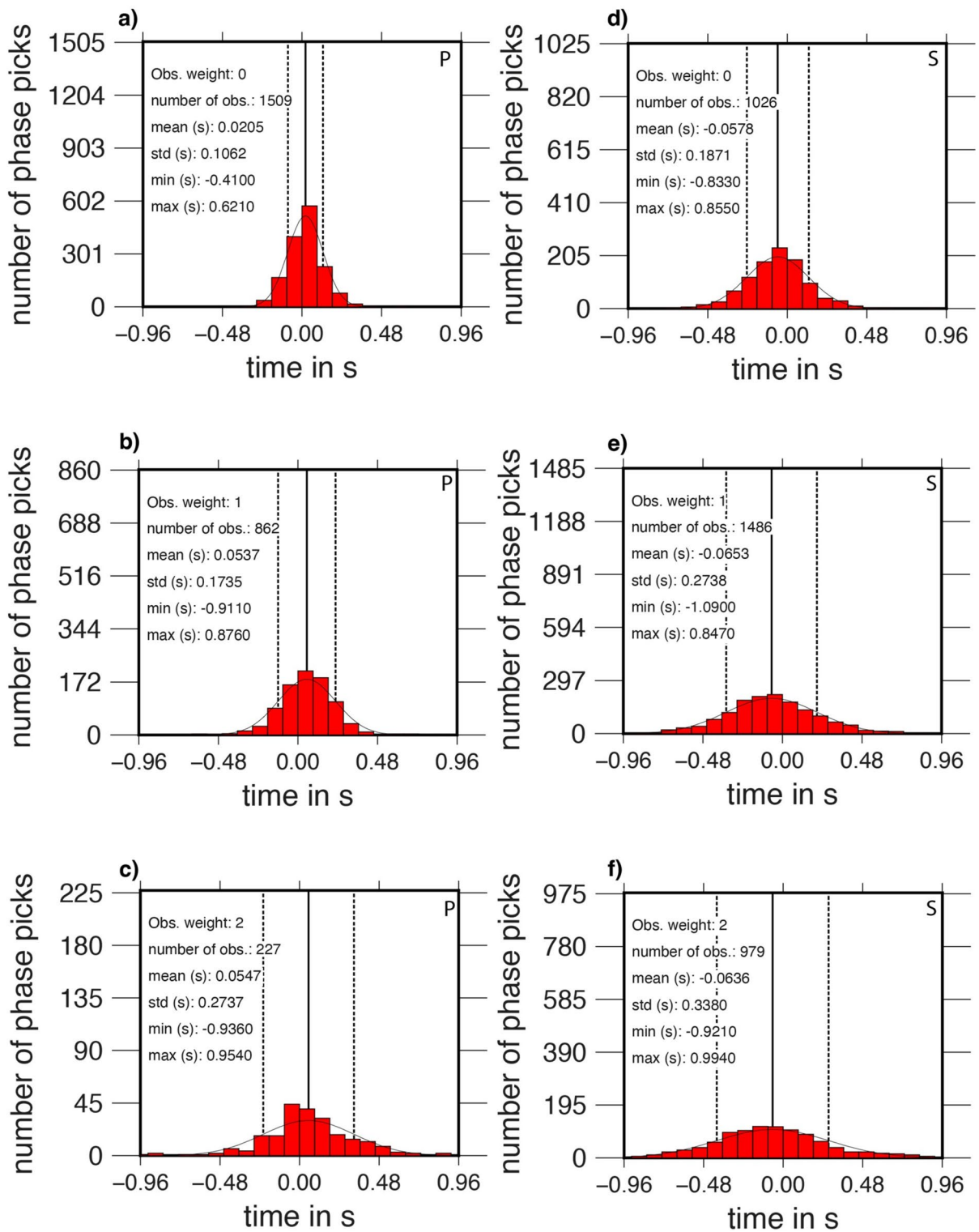


Fig. 7 Statistics of travel time residuals used as input data for the VELEST inversion. As reference the Ahorner (1983) v_p and v_s models (Fig. S1) are used. **a–c** P-wave data for qualities 0, 1, and 2; **d–f** S-wave data for quality classes 0, 1, and 2

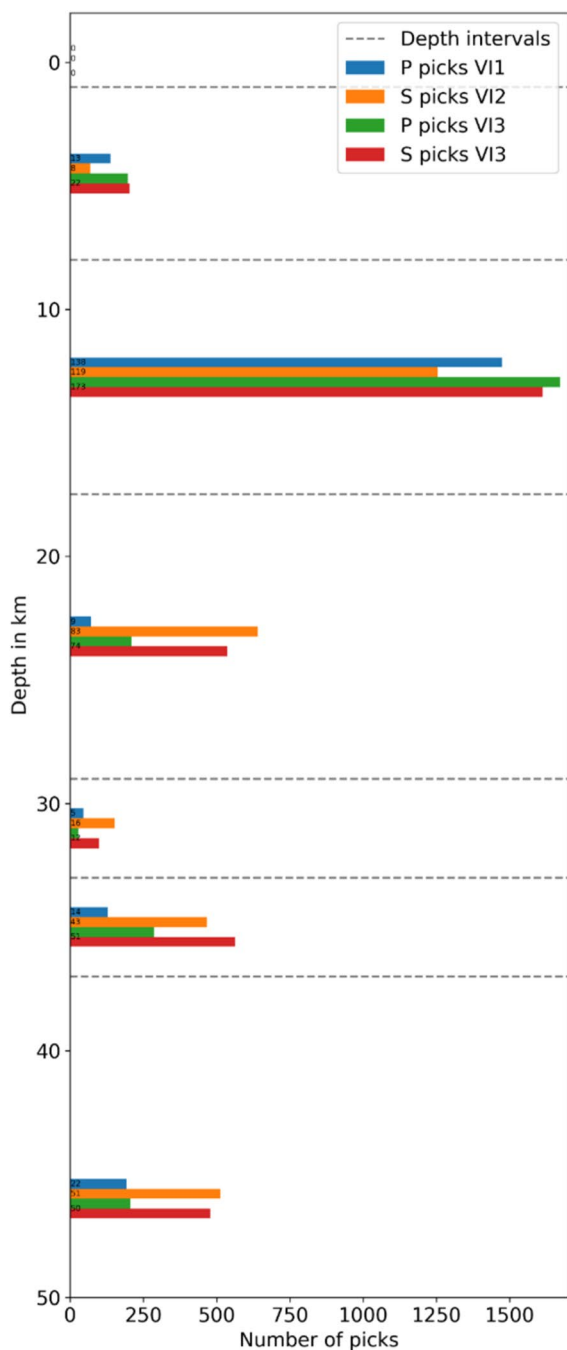


Fig. 8 Distribution of the hypocentre depths of picked seismic phases used for the inversions with VELEST. Blue and orange bars show P- and S-phase counts, respectively, if only P-phases or only S-phases are used for separately determined v_p and v_s models using input VI1 and VI2 (Tab. S5). Green and red bars show P- and S-phase counts, respectively, if both, P- and S-phases, are simultaneously used for the inversion with input VI3 (Tab. S5). The dotted lines indicate the main layers in the study region. The exact numbers of phase picks are given in Table S5

6.2 Inversion strategy

The seismic velocities of the starting models are perturbed 20 times within a range of $\pm 20\%$ to obtain the input models for VELEST, indicated as grey lines in Fig. S2 and Fig. S3. The random velocity perturbations are tested to avoid a dependence of the inversion solution on the starting model. The number, thicknesses, and depths of the layers are varied based on the starting models. For the inversion with VELEST we apply a staggered inversion scheme. First, we invert four times for the velocity models and hypocentre locations. The output velocity models are iteratively used as input for the next inversion run. One inversion run consists of up to 10 iteration steps. During the inversion process we allow the inversion for low-velocity layers, after the first inversion run, if VELEST tries to introduce a low-velocity zone in the first run. Second, after we found a stable velocity structure, a final run inverts for the velocity models, hypocentre locations, and station delay times (again 10 iteration steps). Afterwards we analyse the resolution of the velocity models. Layers which do not converge, due to a lack of earthquakes within the layer, too few hits per layer, an overall short ray length within the layer, or which are too thin, are combined with other layers or are set to seismic velocity values using a priori information from active-source experiments. Such layers are damped in the next modelling step. Furthermore, layers with equal velocities are combined to one layer. Afterwards, a final inversion is conducted for station delay times only.

6.3 Test runs / probing the model space and resolution

To probe the model space and the model resolution we inverted for v_p and v_s separately using the three previously described starting models (Ahorner 1983; Mechie et al. 1983 and the simple three-layer model) and the catalogues VI1 and VI2 as input (Table S5). The input data of the quality classes 0, 1, and 2 (Fig. 7) are assigned weights of 1.0, 0.5, and 0.25. We recognized that the uppermost layer (down to 1 km depth) is poorly constrained, because the inversion models do not converge and/or result in unrealistic seismic velocities. An explanation for this instability may be the short horizontal ray lengths and missing events inside the first layer (Table S5). To account for

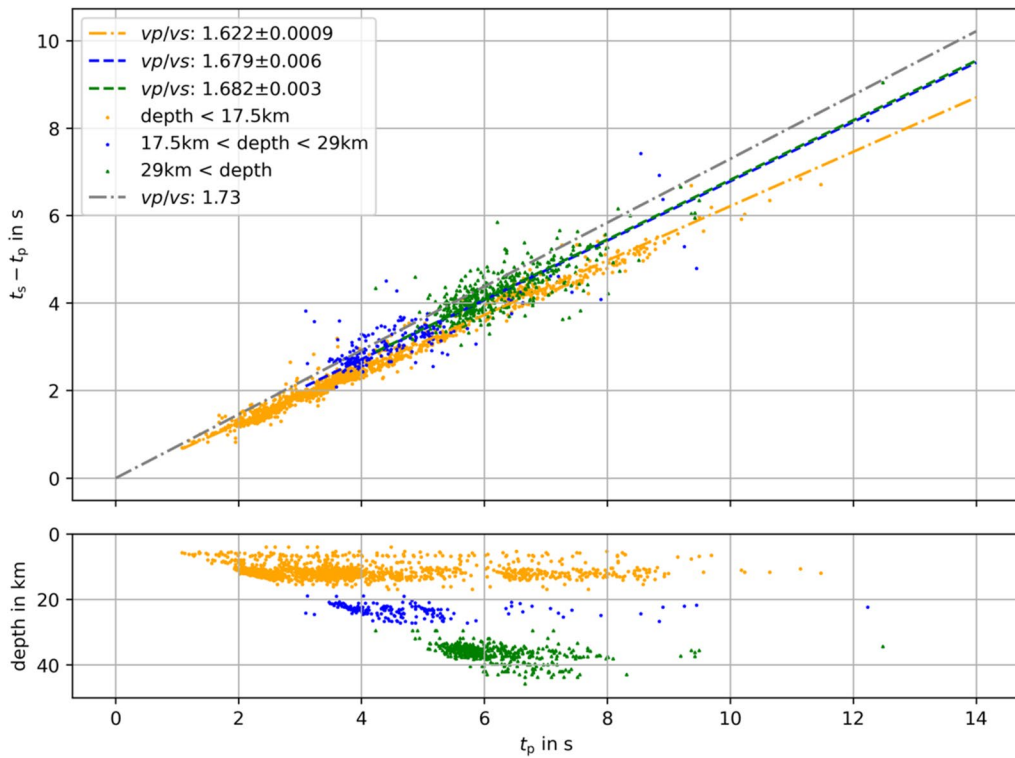


Fig. 9 Wadati diagram with arrival time data of 373 events in the study region. The origin time is taken from a relocation of the events using the v_p and v_s models from Ahorner (1983), see Tab. S1. The gray line represents a v_p / v_s of 1.73 as expected for a standard elastic body with a Poisson’s ratio of 0.5. The dashed lines are fitted v_p / v_s values (Marquardt–Lev-

enberg regression) for events at different hypocentral depths of 0–17.5 km (upper crust, orange), 17.5–29 km (lower crust, blue) and 29–45 km (uppermost mantle, green). The arrival times indicate a decreased v_p / v_s value at depth which slightly increases from 1.62 to 1.68 with depth. The given uncertainties are 1- σ ranges

this problem, we fix v_p to 5.0 km/s in the first layer based on an averaged shallow regional v_p model of Eickhoff (2022) and a v_p / v_s of 1.65 from the Wadati diagram in all following runs, independent of the starting model. Furthermore, below the Moho (29 km depth), the v_p is too low and v_p / v_s does not fit to the values of the Wadati diagram in the uppermost mantle. This is due to the low numbers of events and phases (Table S5), especially for P-waves for which there is only a low number of P-picks from the DLF events (Fig. 8). Thus, we invert with joint P- and S-data (input VI3) with an equal weighting of P- and S-picks, as our catalogue contains more S-picks than P-picks, especially in the lower crust and uppermost mantle. All described inversion results below are the result from joint v_p and v_s inversion using catalogue VI3 as input, if not stated otherwise. After the inversion (four times inversion for velocity and

hypocentres and one run for velocity, hypocentres and station delay times) with our three different starting models, we analyse the output models concerning their RMS, their convergence of the input models and the resulting velocities.

The output RMS values using Ahorner (1983) and Mechie et al. (1983), as well as the two-layer model as input models are quite similar. The output models with the best fit (minimum RMS) have all a very similar RMS value of 0.114–0.119 s (Table S6).

The resulting models after Ahorner (1983) and Mechie et al. (1983) have a similar velocity structure (Fig. S2). The minimum 1-D VELEST models contain a reduction of v_p and v_s in the lower crust compared to the upper crust. Below the Moho (29 km depth), we observe that the models are poorly constrained due to the low numbers of events and phases (Table S5), especially for P-waves. Minimum 1-D

models with the Ahorner (1983) model as starting model, which have one layer in the mantle (half space), converge to low seismic velocities, especially for v_p with just 7.03 km/s (Fig. S2b, Table S1B). Using the finer-layered mantle model from Mechie et al. (1983) the inversion results vary, indicating a resolution problem, again especially for P-waves (Fig. S2 d) due to the low number of rays (Table S5). As we cannot resolve the velocity step at the Moho, especially for v_p , we fix the velocity increase at 29 km depth using the seismic refraction model of Mechie et al. (1983) as a priori information in the following models. We use the long-range seismic refraction model of Mechie et al. (1983) as the depth resolution of this model for the lower crust and upper mantle is better constraint than the one of Ahorner (1983) which has only upper crustal earthquake sources and short epicentral distances.

The simpler starting model with only three layers (near-surface, crust and mantle, Fig. S3 and Table S3) was tested to find averages for v_p and v_s . Using different starting seismic velocities, the results converge to $v_s=3.54$ km/s and $v_p=5.80$ km/s in the crust and $v_s=4.21$ km/s and $v_p=6.67$ km/s in the uppermost mantle. The average crustal v_p / v_s of 1.64 is quite close to the results in the Wadati diagram (Fig. 9). However, the average mantle v_p / v_s of 1.58 (Fig. S3, Table S3) does not coincide with the Wadati diagram, indicating a too low v_p due to resolution problems.

6.4 Models KIT5 and KIT6

6.4.1 KIT5

Based on the resolution and results of the previous inversions we defined a new starting model for another inversion. We use the v_p structure from Mechie et al. (1983) as starting point but include more a priori information. First, we keep the first layer fixed like before with a v_p of 5 km/s after Eickhoff (2022) and a v_p / v_s of 1.65 from the Wadati diagram. Second, we combine layers in the upper crust based on their similar velocities and to simplify the model according to the resolution capabilities of VI3. This results in two layers instead of six layers as in the Mechie et al. (1983) model in the upper crust. The lower boundary of the upper crust is fixed at 17.5 km depth according to the maximum hypocentral depth of the tectonic earthquake hypocenters and

the assumption that the brittle zone coincides with the upper crust. Anyway, variations of ca. ± 2 km of this boundary do not significantly change the inversion results, what is learnt from the results of the previous inversion runs. In Mechie et al. (1983) the boundary between lower and upper crust is in 15 km depth, whereas in Ahorner (1983) it is in 19 km depth (Table S1 and S2). Both inversion results have similar velocity structures in the crust and a similar RMS (Figure S2). The deeper layers are kept according to the model of Mechie et al. (1983). For this reason, the starting models for KIT5 contain five layers in the upper mantle, because the Mechie et al. (1983) model has a complex structure there, including a low-velocity zone (LVZ) with a gradient. As the Mechie et al. (1983) model does not contain v_s , the starting values for v_s in KIT5 are determined from a range of different v_p / v_s values to generate a v_s gradient.

After the inversion process the v_s structure in the crust converges well and even in the mantle the v_s model range is small (Fig. S4). There are two LVZs in the lower crust and upper mantle. The variation of the v_p structure of KIT5 is also small in the crust, but more variable in the mantle. In the mantle v_p has a tendency to unrealistically low values. There are still difficulties in resolving the complicated thin layered structure below the Moho, but we observe a tendency to the model by Mechie et al. (1983) in the KIT5 v_s layer structure. To better constrain v_p in KIT5 we fix the velocities below 29 km depth following the seismic refraction model of Mechie et al. (1983), see Fig. S1, and a v_p / v_s which is adapted to melt and volatiles as suggested by Dahm et al. (2020). In this depth, the subparallel and subvertical ray distribution of our data does not allow to properly determine the fine upper mantle layering or the velocity step related with the Moho, even so the hypocenters are as deep as ca. 45 km. After fixing the velocity structure in the upper mantle we conduct a final inversion run for station delay times only. The resulting lowest RMS deteriorates marginally to 0.115 s (Table S6).

The best model with the lowest RMS (Table S4 and Fig. 11) has low v_p / v_s in the crust and higher v_p / v_s in the mantle. Synthetic Wadati diagrams are given in Fig. S5 and their v_p / v_s values in Table S7. These values, which are averages along the complete ray paths from the source to the mantle, have a similar trend as the observed values with increasing v_p / v_s for deeper hypocenters (Fig. 9).

Table 1 1-D seismic layer model KIT6

depth in km	v_s in km s ⁻¹	v_p in km s ⁻¹	v_p / v_s
-0.9 – 1.0	3.03	5.00	1.65
1.0 – 8.0	3.37	5.69	1.69
8.0 – 17.5	3.78	6.01	1.59
17.5 – 29.0	2.92	4.55	1.56
29.0 – 33.0	4.76	8.10	1.70
33.0 – 37.0	4.50	6.40	1.42
> 37.0	4.38	8.10	1.85

6.4.2 KIT6

As all previous inversions indicate a problem to resolve the thin-layered velocity structure in the upper mantle, especially for v_p , we further simplify the input model of KIT5. This is done to keep all resolvable information in the mantle with our input data. We select a simpler mantle structure with only three layers (Table 1). As a priori information the seismic velocities in the first layer, the Moho depth from Mechie et al. (1983), and the thickness of the upper crust (brittle zone) are kept, like for KIT5. In the following, we describe the results of the inversion for v_p and v_s separately as well as the joint inversion for both.

After the inversion the v_s values converge quite well (Fig. 10a and c) for different starting models. If only S-wave data are used (VI2), there is a LVZ in the crust with a small v_s reduction. If P- and S-wave data are jointly inverted (VI3), then v_s is clearly reduced in the lower crust and there appears a LVZ in the upper mantle which is recovered for all input models. These results agree well with the Mechie et al. (1983) model and the Dahm et al. (2020) model, which also contain a LVZ in the lower crust and in the upper mantle. The v_p results of the inversion are not well resolved (Fig. 10a and d) in the mantle. The v_p result below the Moho contains a gradual increase in velocity with very low velocities in the mantle and no velocity step as in the model by Mechie et al. (1983), which may not be resolvable due the small number of P-phases in this depth range. Furthermore, the expected reduction of v_p below the Moho may also contribute to this problem. Also, the resulting v_p / v_s value of the separate v_p and v_s inversions does not fit the observations of our data from the Wadati diagram (Fig. 9). These arguments lead

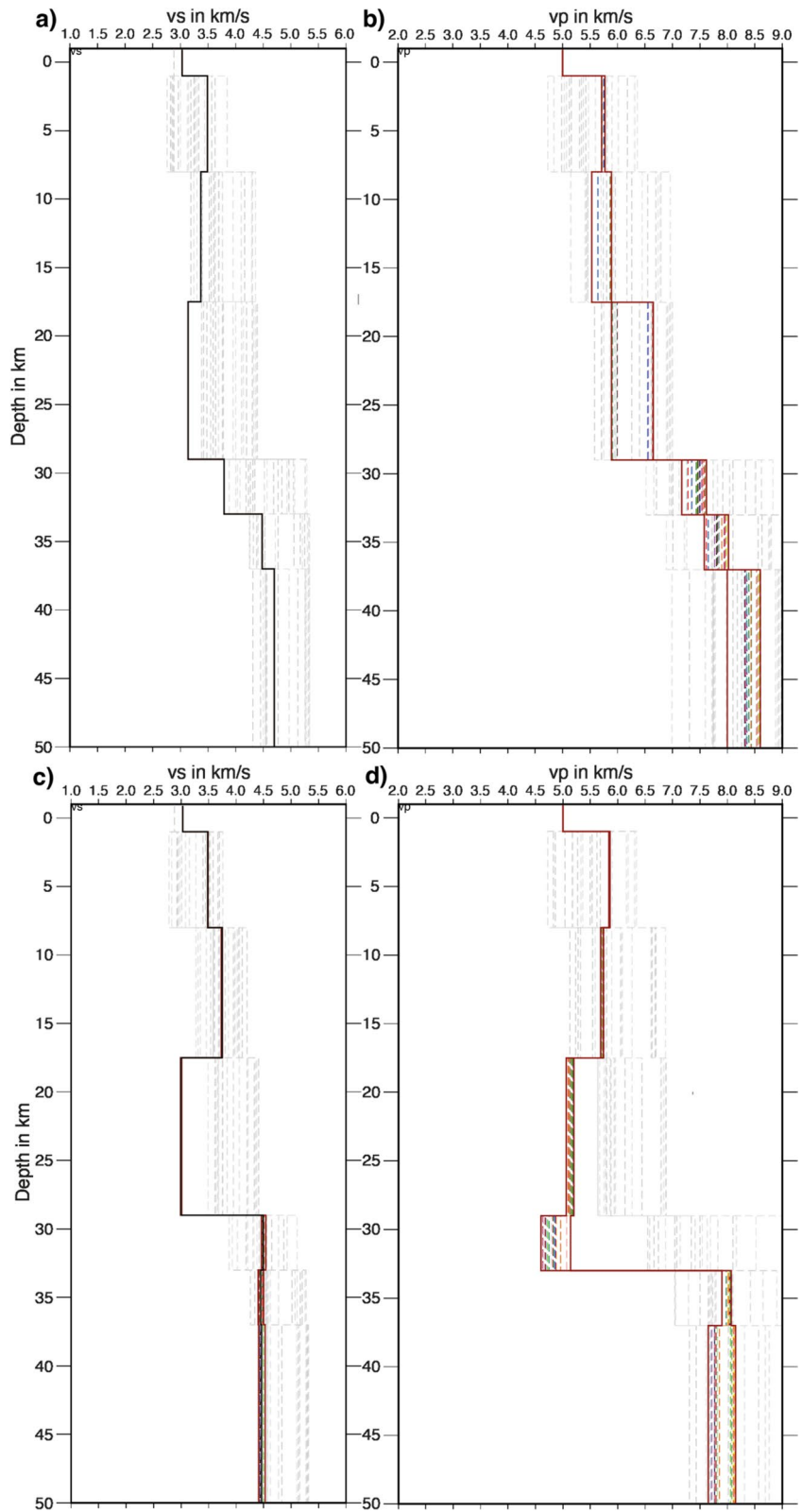
to the conclusion to better use the result of the joint v_p and v_s inversion. As the resolution of v_p is low in the mantle, we fix v_p to a simplified v_p structure after Mechie et al. (1983) which includes a LVZ (Fig. 11). The v_s model is not damped in the mantle and the velocities are the ones determined by the previous inversion runs. Finally, we conduct the last inversion step for station delay times only, with fixed v_p in the mantle.

The resulting lowest RMS values insignificantly vary between 0.114 s and 0.116 s for the KIT6 modelling procedure. The 1-D KIT6 model in Fig. 11 and Table 1 well recovers the v_p / v_s values in the Wadati diagram (Fig. S6 and Table S7). This outcome may give a faint preference for final model KIT6 over final model KIT5 in Fig. 11. Inversion model KIT6 has also three layers less than KIT5, so an overfitting is better avoided. However, we note that the model parameter resolution is influenced by the implemented a priori information for both solutions. As both models achieve a similar low RMS, both can be treated as *pari passu* as long as no further deep-reaching seismic refraction models are available for the EEVF.

6.5 Station delay times

The determined station delay times are presented for the 1-D models KIT5 in Fig. S7 and Table S8, and for KIT6 in Fig. 12 and Table S9. For both models station OCHT is used as reference station and the distribution as well as values of the station terms are very similar. Hence, we only describe Fig. 12. The P-wave station delay times (Fig. 12b) are quite low in the centre of the recording network (<0.2 s) and seem to have a positive NW–SE trend and a negative NE–SW trend relative to OCHT. A similar pattern is observed for the S-wave station delays (Fig. 12a) with slightly higher delay time values compared to the P-wave values. Such an azimuth-dependent pattern may be due to anisotropy, however, the positive delays towards NW may also reflect low seismic velocity in the crust related with the main volcanic centres of the EEVF. At depth there could be still hot magma reservoirs which have a lifetime of several 10,000 years (Schmitt et al. 2022). Overall, the small delay time values of KIT6 in the center of the network (Fig. 12) are interpreted as a hint that the related 1-D v_p and v_s models do well represent the seismic structure below the EEVF. The same holds

Fig. 10 1-D seismic velocity inversion models for KIT6. Gray lines are 21 perturbed input models, colored models are the related inversion results. **a** v_s model from S-wave travel times only (VI1), **b** v_p model from P-wave travel times only (VI2), **c** v_s model from combined P- and S-wave travel times (VI3), **d** v_p model from combined P- and S-wave travel times (VI3)



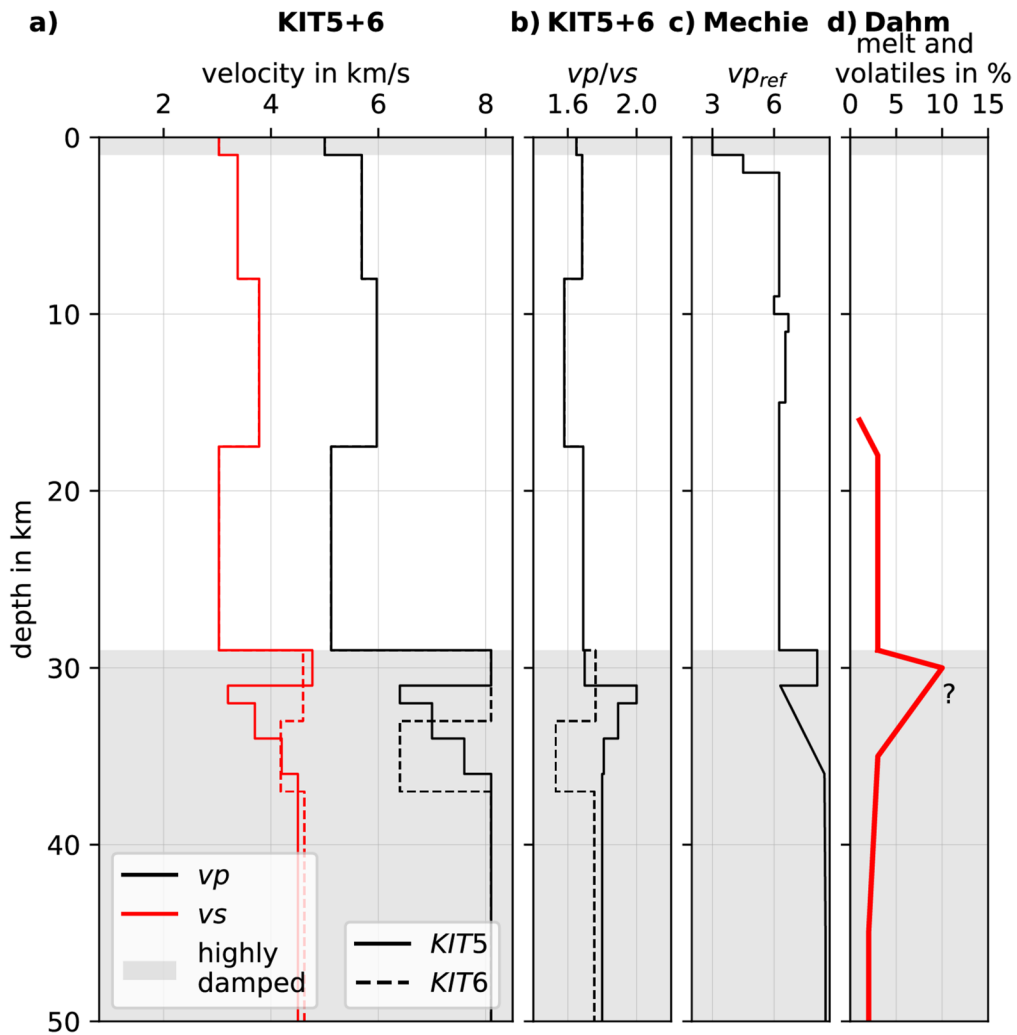


Fig. 11 **a** 1-D seismic v_p and v_s models KIT5 (solid lines) and KIT6 (dashed lines), **b** v_p / v_s , **c** v_p model after Mechie et al. (1983) in the EEVF, **d** proposed melt and volatile distribution

from Dahm et al. (2020). Gray shaded areas indicate depth ranges with poor resolution where v_s and v_p inversion is partly damped and thus based on a priori information (see text)

for the delay times of model KIT5 with its similarly small delay time values.

6.6 Stability test

To evaluate the stability of the minimum 1-D v_p and v_s models KIT5 and KIT6 we conducted shift tests (Kissling et al. 1995) for which we randomly perturbed the input hypocentres in space by up to 0.1° horizontally and by up to 5 km in depth (Figs. S9 – S12). During the inversion runs the velocity model is not damped.

As result of the shift tests, we find that the relocated events differ by less than ca. 2 km in depth and less than ca. 500 m in latitude and longitude relative to our best hypocentre solutions (Fig. S11). The shift tests recover well the sharp line of events along the OFZ, which is aligned NW–SE. The DLF events are shifted back into a channel-like structure underneath the Laacher See Volcano, indicating a clearly confined region of their occurrence. Likewise, the unusual depth of up to ca. 45 km for the DLF events is retrieved by the shift tests. The seismic velocities remain stable, except for the first and

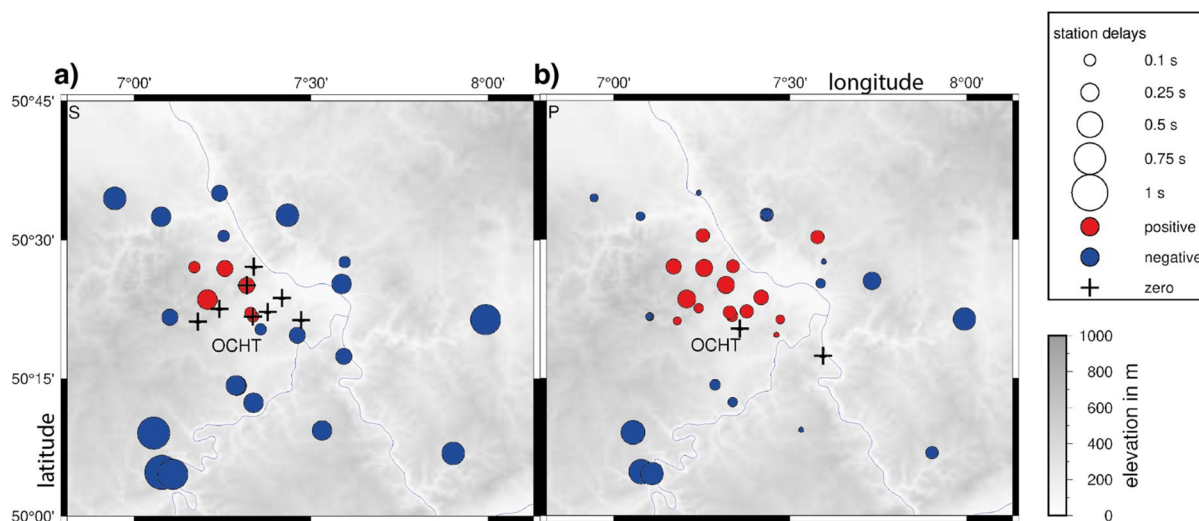


Fig. 12 Station delay times of the 1-D model KIT6 and the DEEP-TEE network. **a** S-waves, **b** P-waves. Station OCHT is the reference station

second layers, as well as the uppermost mantle layer (Fig. S12). The former can be explained, as previously described, by short horizontal ray lengths in these layers. The Moho region cannot be resolved, due to the complicated structure, enclosed by two LVZs. These three layers are also the ones with the smallest event numbers. Hence the inclusion of the a priori information is necessary to fix the velocity models below the crust.

6.7 Relocation of event catalog

The relocation result with the 1-D model KIT6 in Fig. 13 displays a clearer picture of the seismicity distribution compared to the routine event locations. The earthquakes along the OFZ are more closely together and outline a sharp active fault with NW–SE strike (Fig. 13). The hypocentres of the tectonic events (dots) are as deep as ca. 17–18 km which corresponds to the depth range of the seismogenic zone typical for Germany (BGR Kataloge 2023). The distribution of the DLF seismicity (stars in Fig. 13) seems to be confined to a less than 10 km wide zone just SE of LSV as found in Hensch et al. (2019). This zone steeply crosses the crust and the lower lithosphere and reaches the asthenosphere at about 45 km depth (Mathar et al. 2006; Seiberlich et al. 2013).

7 Discussion and preliminary results

The *DEEP-TEE* experiment provides valuable seismological data which confirm the occurrence of unusually deep earthquakes in the upper mantle underneath the EEVF in the midst of Central Europe, as first described by Stange et al. (2014) and Hensch et al. (2019). The earthquake catalog of the University of Cologne, earthquake station Bensberg, reported an event in the mantle at already in September 2011 (<http://www.seismo.uni-koeln.de/catalog/2011.htm>). Such intra-plate seismicity in the lithospheric mantle is seldomly observed and due to its spatial coincidence, we argue for a strong causal relationship with the dormant volcanic field in the East Eifel.

To improve the event locations in the EEVF, we invert the picked P-wave and S-wave phase arrival times for 1-D v_p and v_s models KIT5 and KIT6 (Fig. 11) including station delay times (Fig. S7 and Fig. 12). Both, KIT5 and KIT6, equally well fit the input data. KIT5 and KIT6 consist of an upper crust with increasing seismic velocities with depth and a LVZ in the lower crust. As the ray distribution does not allow a unique solution for v_p and v_s below the Moho, we add a priori information after Mechie et al. (1983) and Dahm et al. (2020). The differences between KIT5 and KIT6 are small, however, we slightly prefer KIT6,

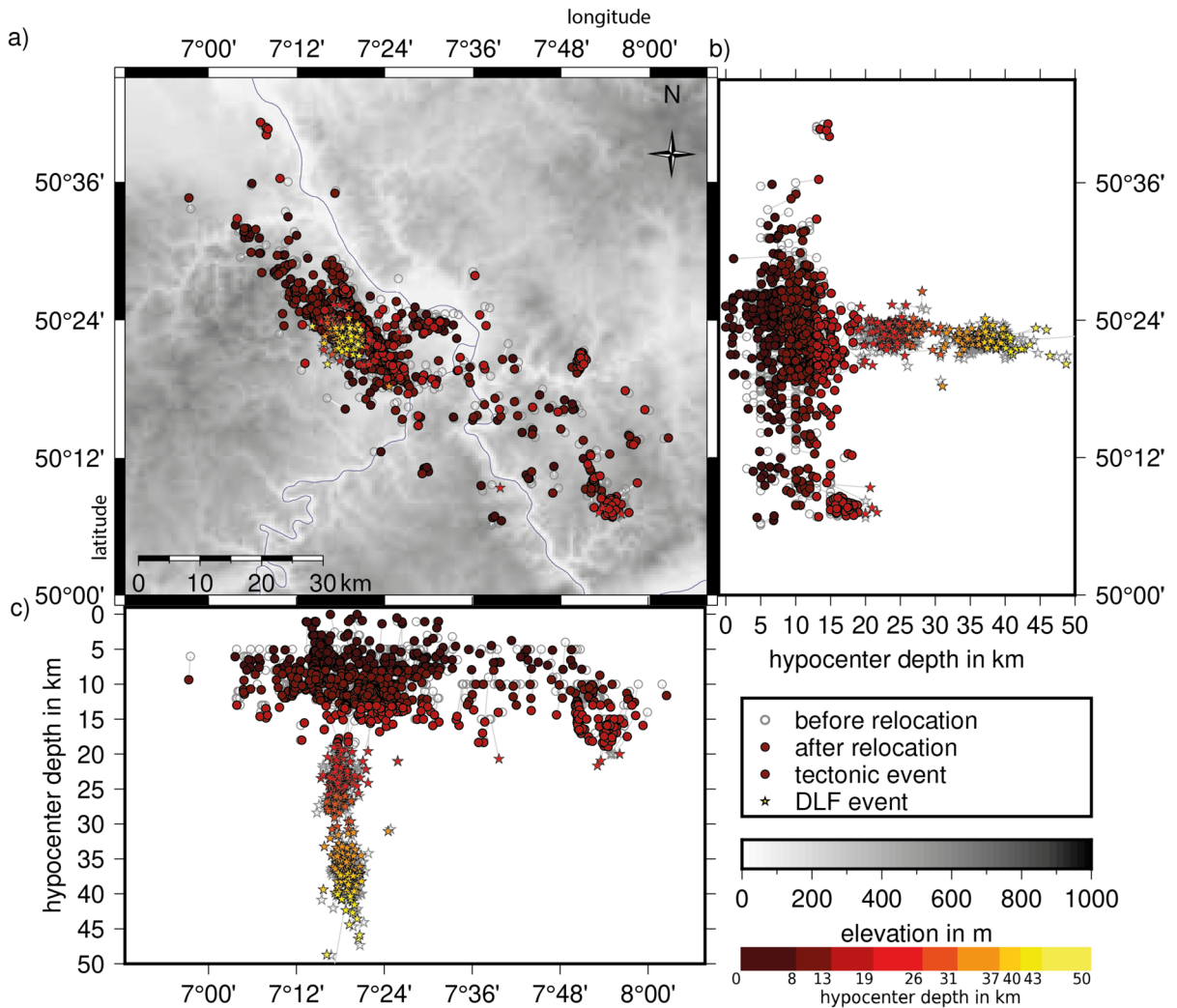


Fig. 13 Relocation result for the 1325 input events using the 1-D v_p and v_s models KIT6 (Fig. 11) incl. station delay times from Fig. 12. The starting hypocenters are from the bulletins of the state seismological service and from own preliminary loca-

tions, especially for DLF events. Circles show tectonic events, stars indicate DLF events; colour indicates hypocentral depth with a color scale adjusted to Hensch et al. (2019)

because it has fewer layers and, therefore, better avoids an overfitting of the data. This is in accordance with the often used principle of Occom’s razor (De Groot-Hedlin and ConsTable 1990).

The two LVZs can be explained with partial melt and volatiles in the lower crust and upper mantle (Fig. 11d, Dahm et al. 2020). A depth-dependent low v_p / v_s is observed in the data (Fig. 9) and this is reproduced with the models KIT5 and KIT6. The low v_p / v_s could be a hint for volcanic gas in the upper crust (Dvorkin et al. 1999) which is consistent with the observation of volcanic gas emissions at the

surface (Bräuer et al. 2013; Goepel et al. 2015). The P- and S-wave station delay times reveal a positive NW–SE and a negative NE–SW trend. The positive delays towards NW hint to lower seismic velocities in the crust in the area of the volcanic centres of the EEVF relative to the seismic velocities in KIT5 and KIT6. This is another indicator for increased temperature and/or melt and volatiles in the crust (Paulatto et al. 2022 and references therein). For an improved petrophysical interpretation a 3-D velocity model including v_p / v_s is necessary to discriminate between temperature, melt, fluids and gases.

The systematic analysis of the low frequency events between 2014 and 2018 revealed that they have deeper hypocentres (about 8–45 km depth) than the known tectonic crustal seismicity (mainly 5–17 km depth) with higher frequency waves (Hensch et al. 2019). In addition, Hensch et al. (2019) observe a slight increase of the corner frequency of the DLF events with depth and, therefore, argue that the low-frequency content is not a filter effect along the propagation path between source and receiver. The waveforms of the DLF events are similar to recordings from other active volcanic regions world-wide and, therefore, they are interpreted as signals related to ongoing deep magmatic processes. Combining the recordings from permanent and mobile seismological stations allows us now to well locate many events below the Moho (Fig. 13). The refined locations of the ca. 200 DLF events ($ML < 1.5$) between 2014 and 2021 using the local vp and vs models KIT5 and KIT6 visualise a nearly continuous depth distribution of the DLF events. This distribution seems to represent a translithospheric magmatic channel southeast of Laacher See Volcano (Fig. 13) which may be related with a very slow refilling of crustal magma reservoirs with melt and/or volatiles (Koushesh et al. in prep). During the time period 2014–2021 there is no systematic temporal or spatial migration of the DLF events. Perhaps such migrations may occur at longer time scales which cannot be resolved yet.

Tectonic activity is limited to the upper ca. 17 km depth, in accordance with a regional model in which strength resides in one layer (Jackson 2002; Jackson et al. 2021). This behaviour should be modelled in more details, using the numerous temperature and lithology data from the Eifel region. The continual tectonic activity at the Ochtendung Fault Zone (OFZ) can be used to image its actual fault plane (Fig. 13 and Fig. S8). A preliminary model proposes a near-vertical fault which is active between ca. 5 km and 15 km depth (Föst et al. 2022) and will be complemented with fault plane solutions. The occurrence of swarm-like shallow activity in the north of LSV (Hensch et al. 2019) is not yet analysed in detail, but the DEEP-TEE data may help in the future to outline possible fluid pathways at depth in this area. The many different seismic signals in the EEVF require more studies to better understand the ongoing magmatic and tectonic processes and its consequences, including a robust hazard analysis. Therefore, we will continue the operation of the

DEEP-TEE experiment. There are also other ongoing seismic experiments in the EEVF. In 2020/2021 a ca. 4.5 km long line of 17 recording stations was running ca. 8 km southeast of LSV to study the OFZ. During June 2021 additional 200 instruments were placed on this line at 5 m distances during an active source experiment with an accelerated drop weight which was dropped at 25 m shot distances (Haupt et al. 2022). For an additional high-resolution study, a large-N seismological network recorded between summer 2022 and summer 2023 (Dahm et al. 2022a, b) which will hopefully add more data to resolve the crustal structure underneath the EEVF in hitherto unprecedented resolution.

8 Conclusions

The seismological DEEP-TEE experiment is a significant contribution to monitor the dormant magmatic-volcanic system of the Laacher See Volcano and the East Eifel Volcanic Field. Despite problems with high cultural seismic noise, a sensitive recording network was installed which records local events with magnitudes below ML 1 in the uppermost mantle. The new seismic velocity models (vp , vs , vp / vs) including stations correction terms allow us to well locate these events what is the basis for geodynamic and magmatic studies. The determined low-seismic velocity in the lower crust and upper mantle is interpreted as signs for volatiles or melt. The located deep low-frequency events outline a narrow 3-D structure (Fig. 13). This structure reaches downwards some 15 km underneath the Moho representing the deepest seismicity in Central Europe. It is interpreted as a translithospheric magmatic channel which may feed a crustal magma reservoir from as deep as the asthenosphere or rather the top of the low velocity anomaly related with the Eifel plume (Mathar et al. 2006; Seiberlich et al. 2013). Based on petrological analysis of the rock material that was brought to the surface during the last eruption of the LSV, the lifetime of such a crustal reservoir may last some 10,000 years (Rout and Wörner 2018; Schmitt et al. 2022) before the occurrence of another eruption in the far future.

Acknowledgements The seismological DEEP-TEE experiment is financed by internal sources of the Karlsruhe Institute of Technology, Landesamt für Geologie und Bergbau

Rheinland-Pfalz, and Deutsches GeoForschungsZentrum Potsdam. Felix Bögelspacher, David Madeja, Leon Merkel, Werner Scherer, and Ulf Wolfstädter helped with the station installation in the field; Michael Frietsch and Rainer Plokarz helped with processing at the KABBA datacentre. Numerous local authorities, companies and private people helped with sites for instrument installation and power supply including the municipalities of Bendorf, Emmelshausen, Mendig, Niederbreitscheid, Rengsdorf, Sinzig and Weißenthurm, Wasserversorgungszweckverband Maifeld-Eifel, Kreiswasserwerke Cochem-Zell, Bahner Hof, Deutsche Vulkanologische Gesellschaft, Pymont Castle, St. Hubertus Schützenbruderschaft e.V. 1863 Miesenheim, Propstei Buchholz, Hüttenhof, Möchsheide Airfield, TRIWO Gewerbetpark Mendig, Luftsportverein Mönchsheide e.V., Kunst- und Kulturkreis Erpel, Grube Bendisberg, Obst- und Gartenbau Levermann.

Instruments have been provided by the Geophysical Instrument Pool at GFZ Potsdam, Karlsruhe BroadBand Array at KIT Karlsruhe, and Geological Survey of Rhineland-Palatinate in Mainz. Additional waveforms from permanent stations are used from the Seismological Service at the Geological Survey of North Rhine—Westphalia (GDNRW, FDSN network code NH), and the German Regional Seismic Network (GR) operated by the Federal Institute for Geosciences and Natural Resources (BGR, Germany). Maps are plotted with GMT (Wessel et al. 2019). Three anonymous reviewers provided supporting comments and suggestions to improve the manuscript. F. Wenzel and A. Rietbrock are thanked for continuous support.

Authors' contributions Joachim Ritter and Bernd Schmidt coordinated the field work and the network design. Konun Koushesh, Jan-Phillip Föst and Martin Hensch analysed the seismic recordings. Konun Koushesh, Joachim Ritter and Martin Hensch worked on the detection of the deep low frequency seismicity. Jan-Phillip Föst, Julian Bühler, Sarah Mader and Joachim Ritter determined the 1-D velocity models and hypocenters. All authors were involved in preparing the manuscript text and figures.

Funding Open Access funding enabled and organized by Projekt DEAL. K.K. was supported with a grant from the Ministry of Science, Research and Arts Baden-Württemberg (Az.: 31–7547.223–10/8/1)) and had a grant from the STI-BET DAAD Pre-Graduation Scholarship. S.M. was supported by a grant of the Deutsche Forschungsgemeinschaft (DFG, RI1133/13–1).

Data availability The waveform data from 2014 to 2016 is available at GFZ: <https://geofon.gfz-potsdam.de/doi/network/1P/2014> (Ritter et al. 2014). The BGR recordings are available through EIDA (FDSN code GR). The recordings from the permanent recording stations with FDSN codes LE and NH are available at the data centers given on the related FDSN webpages.

Declarations

Conflict of interest The authors declare no competing interests.

Open Access This article is licensed under a Creative Commons Attribution 4.0 International License, which permits use, sharing, adaptation, distribution and reproduction in any medium or format, as long as you give appropriate credit to the original author(s) and the source, provide a link to the Creative Commons licence, and indicate if changes were made. The images or other third party material in this article are included in the article's Creative Commons licence, unless indicated otherwise in a credit line to the material. If material is not included in the article's Creative Commons licence and your intended use is not permitted by statutory regulation or exceeds the permitted use, you will need to obtain permission directly from the copyright holder. To view a copy of this licence, visit <http://creativecommons.org/licenses/by/4.0/>.

References

- Ahorner L (1983) Historical seismicity and present-day microearthquake activity of the Rhenish Massif, Central Europe. In: Fuchs K, von Gehlen K, Mälzer H, Murawski H, Semmel A (eds) Plateau Uplift. Springer, Berlin, pp 198–221
- Bonnefoy-Claudet S, Cotton F, Bard P-Y (2006) The nature of noise wavefield and its applications for site effects studies - a literature review. *Earth-Sci Rev* 79:205–227. <https://doi.org/10.1016/j.earscirev.2006.07.004>
- Bormann P (1998) Conversion and comparability of data presentations on seismic background noise. *J Seismol* 2:37–45. <https://doi.org/10.1023/A:1009780205669>
- Brace WF, Kohlstedt DL (1980) Limits on lithospheric stress imposed by laboratory experiments. *J Geophys Res* 85(B11):6248–6252. <https://doi.org/10.1029/JB085iB11p06248>
- Bräuer K, Kämpf H, Niedermann S, Strauch G (2013) Indications for the existence of different magmatic reservoirs beneath the Eifel area (Germany): a multi-isotope (C, N, He, Ne, Ar) approach. *Chem Geol* 356:193–208. <https://doi.org/10.1016/j.chemgeo.2013.08.013>
- Cloetingh S, Koptev A, Lavecchia A, Kovács IJ, Beekman F (2022) Fingerprinting secondary mantle plumes. *Earth Planet Sci Lett* 597:117819. <https://doi.org/10.1016/j.epsl.2022.117819>
- Dahm T, Stiller M, Mechie J, Heimann S, Hensch M, Woith H, Schmidt B, Gabriel G, Weber M (2020) Seismological and geophysical signatures of the deep crustal magma systems of the Cenozoic volcanic fields beneath the Eifel, Germany. *Geochem Geophys Geosyst* 21:e2020GC009062. <https://doi.org/10.1029/2020GC009062>
- Dahm T, Milkereit C, Isken M, Cesca S, Yuan X, Sens-Schönfelder C, Tilmann F, Pilz M, Cotton F, Woith H, Krawczyk C, Haberland C, Hensch M, Schmidt B, Endrun-Knapmeyer B, Meier T, de Siena L, van Camp M, Lecocq T, Oth A (2022a) Ein seismologisches Großexperiment zur Untersuchung magmatischer Prozesse unter der Eifel. Jahrestagung Deutsche Geophysikalische Gesellschaft, Tagungsband (Proceedings), Munich, PS-G.05, p 211

- Dahm T et al (2022b) Vulkanseismologisches Experiment in der Eifel. <https://www.gfz-potsdam.de/sektion/erdbeben-und-vulkanphysik/projekte/eifel-vulkanseismologisches-experiment/>. Accessed 19 September 2024
- De Groot-Hedlin C, Constable SC (1990) OCCAM's inversion to generate smooth, two-dimensional models from magnetotelluric data. *Geophysics* 55:1613–1624. <https://doi.org/10.1190/1.1442813>
- Demoulin A, Hallot E (2009) Shape and amount of the Quaternary uplift of the western Rhenish shield and the Ardennes (western Europe). *Tectonophysics* 474:696–708
- Diehl T, Kissling E, Bormann P (2012) Tutorial for consistent phase picking at local to regional distances. In: Bormann P (Ed.) *New Manual of Seismological Observatory Practice 2 (NMSOP-2)*. Deutsches GeoForschungsZentrum GFZ Potsdam, 1–21. https://doi.org/10.2312/GFZ.NMSOP-2_IS_11.4
- Dvorkin J, Mavko G, Nur A (1999) Overpressure detection from compressional- and shear-wave data. *Geophys Res Lett* 26(22):3417–3420. <https://doi.org/10.1029/1999GL008382>
- Eickhoff D (2022) Abbildung der Krustenstruktur im Bereich der Eifel durch Reprozessierung der tiefenseismischen Profile DEKORP87–1A/1B. University of Freiberg, Master thesis, 94 pp
- Föst J-P, Bühler J, Koushesh M, Mader S, Ritter J, Hensch M, Schmidt B (2022) New 1-D seismic velocity models and hypocentres in the East Eifel Volcanic Field. Jahrestagung Deutsche Geophysikalische Gesellschaft, Tagungsband (Proceedings), Munich, PS-C.28, p 141
- GEOFON (1997–1998) The XE Seismic Network, 1997–1998. <https://geofon.gfz-potsdam.de/waveform/archive/network.php?ncode=XE&year=1997>. Accessed 19 September 2024
- Goepel A, Lonschinski M, Viereck L, Büchel G, Kukowski N (2015) Volcano-tectonic structures and CO₂-degassing patterns in the Laacher See basin, Germany. *Int J Earth Sci* 104:1483–1495. <https://doi.org/10.1007/s00531-014-1133-3>
- Greve A, Stange S, Brüstle W (1999) Datenerfassung und –verarbeitung im Erdbebendienst. Landesamt Geol Rohst Bergb Baden–Württ, Freiburg i. Br., Informationen 11: 25–32 https://www.google.com/url?sa=t&source=web&rc=j&opi=89978449&url=https://produkte.lgrb-bw.de/docPool/c223_data.pdf&ved=2ahUKEwjyXj61GHAXV A3gIHHaR7ACIQFnoECBEQAQ&usq=AOvVaw1Wq2gRfq6S8aBPuNNc7TeG Accessed 28 June 2024
- Hensch M, Dahm M, Ritter J, Heimann S, Schmidt B, Stange S, Lehmann K (2019) Deep low-frequency earthquakes reveal ongoing magmatic recharge beneath Laacher See Volcano (Eifel, Germany). *Geophys J Int* 216:2025–2036. <https://doi.org/10.1093/gji/ggy532>
- Hinzen K-G (2003) Stress field in the Northern Rhine area, Central Europe, from earthquake fault plane solutions. *Tectonophysics* 377:325–356. <https://doi.org/10.1016/j.tecto.2003.10.004>
- Hinzen K-G, Reamer SK, Fleischer C (2021) Seismicity in the Northern Rhine Area (1995–2018). *J Seismol* 25:351–367. <https://doi.org/10.1007/s10950-020-09976-7>
- Haupt L, Frietsch M, Rietbrock A, Ryberg T, Haberland C, Ritter J, Schmidt B, Reicherter K, Hertweck T (2022) The active Ochtendung Fault Zone Seismic Experiment – shallow refraction tomography in the East Eifel Volcanic Field, Germany. European Geosciences Union, General Assembly, EGU22-9800, 10.5194/egusphere-egu22-9800. Accessed 01 December 2022
- IASPEI (2013) Summary of Magnitude Working Group recommendations on standard procedures for determining earthquake magnitudes from digital data. http://www.iaspei.org/commissions/CSOI/Summary_WG_recommendations_20130327.pdf. Accessed 01 December 2022
- Jackson J (2002) Strength of the lithosphere. *GSA Today* 12(9):4–10
- Jackson J, McKenzie D, Priestley K (2021) Relations between earthquake distributions, geological history, tectonics and rheology on the continents. *Phil Trans R Soc A* 379:20190412. <https://doi.org/10.1098/rsta.2019.0412>
- Kataloge BGR (2023) https://www.bgr.bund.de/DE/Themen/Erdbeben-Gefahrungsanalysen/Seismologie/Seismologie/Erdbebenausswertung/Erdbebenkataloge/Kataloge_Bulletins/kataloge_bulletins_node.html. Accessed 01 Sept 2023
- Keyser M, Ritter JRR, Jordan M (2002) 3D shear-wave velocity structure of the Eifel plume. *Earth Planet Sci Lett* 203:59–82
- Kissling E, Ellsworth WL, Eberhart-Phillips D, Kradolfer U (1994) Initial reference models in local earthquake tomography. *J Geophys Res* 99(B10):19635–19646
- Kissling E, Kradolfer U, Maurer, H (1995) Program VELEST user 's guide – Short Introduction. Institute of Geophysics, ETH Zürich. <https://seg.ethz.ch/software/velest.html> Accessed 01 December 2022
- Koushesh K, Ritter J (2024) An adaptive 6-dimensional floating-search multi-station seismic-event detector (A6-DFMSD) and its application to low-frequency earthquakes in the East Eifel Volcanic Field, Germany. *J Appl Volcanol* (in print)
- Kreemer C, Blewitt G, Davis PM (2020) Geodetic evidence for a buoyant mantle plume beneath the Eifel volcanic area, NW Europe. *Geophys J Int* 222:1316–1332. <https://doi.org/10.1093/gji/ggaa227>
- Landeserdbebendienst (2018) Bulletin Files, Az. 4784/21_8714, Az. 4784/19_12333. <https://erdbeben.led-bw.de/> Accessed 19 September 2024
- Leder J, Wenzel F, Daniell JE, Gottschämmer E (2017) Loss of residential buildings in the event of a re-awakening of the Laacher See Volcano (Germany). *J Volcanol Geotherm Res* 337:111–123. <https://doi.org/10.1016/j.jvolgeores.2017.02.019>
- Leydecker G (2011) Erdbebenkatalog für Deutschland mit Randgebieten für die Jahre 800 bis 2008. Geologisches Jahrbuch Reihe E 59, Schweizerbart, Stuttgart, 198 pp. ISBN 978–3–510–95989–1
- Mathar JP, Ritter JRR, Friederich W (2006) Surface waves image the top of the Eifel plume. *Geophys J Int* 164(2):377–382. <https://doi.org/10.1111/j.1365-246X.2006.02835.x>
- McNutt SR, Thompson G, Johnson J, De Angelis S, Fee D (2015) Seismic and infrasonic monitoring. In: Sigurdsson H, Houghton B, McNutt SR, Rymer H, Stix J (eds.) *The Encyclopedia of Volcanoes*. Academic Press, London, pp

- 1071–1099. <https://doi.org/10.1016/B978-0-12-385938-9.00063-8>
- Mechie J, Prodehl C, Fuchs K (1983) The long-range seismic refraction experiment in the Rhenish Massif. In: Fuchs K, von Gehlen K, Mälzer H, Murawski H, Semmel A (eds) *Plateau Uplift*. Springer, Berlin, pp 261–274
- Mertz DF, Löhnertz W, Nomaded S, Pereira A, Prelevića D, Renne PR (2015) Temporal–spatial evolution of low-SiO₂ volcanism in the Pleistocene West Eifel volcanic field (West Germany) and relationship to upwelling asthenosphere. *J Geodyn* 88:59–79. <https://doi.org/10.1016/j.jog.2015.04.002>
- Meyer W (2013) *Geologie der Eifel*, 4th edn. Schweizerbart'sche Verlagsbuchhandlung, Stuttgart, p 704
- Meyer W, Stets J (2007) Quaternary uplift in the Eifel Area. In: Ritter JR, Christensen UR (eds) *Mantle Plumes — A Multidisciplinary Approach*. Springer, Heidelberg, pp 369–378
- Ochmann N (1988) Tomographische Analyse der Krustenstruktur unter dem Laacher-See-Vulkan mit Hilfe von teleseismischen Laufzeitresiduen. Dissertation, RWTH Aachen 106pp
- Pallister J, Mc Nutt SR (2015) Synthesis of volcano monitoring. In: Sigurdsson H, Houghton B, McNutt SR, Rymer H, Stix J (eds) *The Encyclopedia of Volcanoes*. Academic Press, London, pp 1151–1171. <https://doi.org/10.1016/B978-0-12-385938-9.00066-3>
- Park C, Schmincke H-U (2020) Multistage damming of the Rhine River by tephra fallout during the 12,900 BP Plinian Laacher See Eruption (Germany). *Syn-eruptive Rhine damming I*. *J Volcanol Geotherm Res* 389:106688. <https://doi.org/10.1016/j.jvolgeores.2019.106688>
- Paulatto M, Hoofft EEE, Chrapkiewicz K, Heath B, Toomey DR, Morgan JV (2022) Advances in seismic imaging of magma and crystal mush. *Front Earth Sci* 10:970131. <https://doi.org/10.3389/feart.2022.970131>
- Pelzing R (2008) Erdbeben in Nordrhein-Westfalen. *Geologischer Dienst NRW, Krefeld*, ISBN 978–3–86029–971–5
- Peterson J (1993) Observations and modeling of seismic background noise. U.S. Geological Survey, Open-File report 93–322, 95 pp
- Plesinger A, Hellweg M, Seidl D (1986) Interactive high-resolution polarization analysis of broad-band seismograms. *J Geophysics* 59:129–139
- Raikes S, Bonjer K-P (1983) Large-scale mantle heterogeneity beneath the Rhenish Massif and its vicinity from teleseismic P-residuals measurements. In: Fuchs K, von Gehlen K, Mälzer H, Murawski H, Semmel A (eds) *Plateau Uplift*. Springer, Berlin, pp 315–331
- Reinig F, Wacker L, Jöris O, Oppenheimer C, Guidobaldi G, Nievergelt D, Adolphi F, Cherubini P, Engels S, Esper J, Land A, Lane C, Pfanzen H, Remmele S, Sigl M, Sookdeo A, Büntgen U (2021) Precise date for the Laacher See eruption synchronizes the Younger Dryas. *Nature* 595:66–69. <https://doi.org/10.1038/s41586-021-03608-x>
- Ritter JRR, Achauer U, Christensen UR, Eifel Plume Team (2000) The teleseismic tomography experiment in the Eifel Region, Central Europe: design and first results. *Seismol Res Lett* 71:437–443. <https://doi.org/10.1785/gssrl.71.4.437>
- Ritter JRR, Jordan M, Christensen UR, Achauer U (2001) A mantle plume below the Eifel volcanic fields, Germany. *Earth Planet Sci Lett* 186:7–14. [https://doi.org/10.1016/S0012-821X\(01\)00226-6](https://doi.org/10.1016/S0012-821X(01)00226-6)
- Ritter JRR, Schmidt B, Haberland C, Weber M (2014) DEEP TEE. GFZ Data Services (other / seismic network). <https://geofon.gfz-potsdam.de/doi/network/1P/2014>. Accessed 19 Sept 2024
- Rout SS, Wörner G (2018) Zoning and exsolution in alkali feldspars from Laacher See volcano (Western Germany): constraints on temperature history prior to eruption. *Contrib Mineral Petrol* 173:95. <https://doi.org/10.1007/s00410-018-1522-x>
- Schmincke HU (2007) The Quaternary volcanic fields of the East and West Eifel (Germany). In: Ritter JRR, Christensen UR (eds) *Mantle Plumes*. Springer, Berlin, pp 241–322. https://doi.org/10.1007/978-3-540-68046-8_8
- Schmitt FH, Schmitt AK, Gerdes A, Harvey JC (2022) Magma accumulation underneath Laacher See volcano from detrital zircon in modern streams. *J Geol Society* 180. <https://doi.org/10.1144/jgs2022-064>
- Schreiber U, Jentzsch G (2021) Vulkanische Gefährdung in Deutschland. BGE-Vergabenummer: SEVGV3T-19–04-OI. https://www.bge.de/fileadmin/user_upload/Standortsuche/Forschung/Bericht_-_Vulkanische_Gefae_hrdung_in_Deutschland_barrierefrei.pdf. Accessed 19 Sept 2024
- Seiberlich CA, Ritter JRR, Wawerzinek B (2013) Topography of the lithosphere-asthenosphere boundary below the Upper Rhine Graben Rift and the volcanic Eifel region, Central Europe. *Tectonophysics* 603:222–236. <https://doi.org/10.1016/j.tecto.2013.05.034>
- Shelly DR, Skoumal RJ, Hardebeck JL (2022) S/P amplitude ratios derived from single-component seismograms and their potential use in constraining focal mechanisms for microearthquake Sequences. *The Seismic Record* 2(2):118–126. <https://doi.org/10.1785/0320220002>
- Stammler K, Bischoff M, Brüstle A, Ceranna L, Donner S, Fischer K, Gaebler P, Friederich W, Funke S, Hartmann G, Homuth B, Knapmeyer-Endrun B, Korn M, Megies T, Pilger C, Plenefisch T, Pustal I, Rappsilber I, Schmidt B, Sonnabend L, Stange S, Wassermann J, Wegler U (2021) German seismic and infrasound networks contributing to the European Integrated Data Archive (EIDA). *Seismol Res Lett* 92:1854–1875. <https://doi.org/10.1785/0220200401>
- Stange S, Kurrle D, Dahm T, Hinzen K-G, Lehmann K, Ritter JRR, Schmidt B (2014) Subkrustale Seismizität in der Osteifel. *Jahrestagung Deutsche Geophysikalische Gesellschaft, Tagungsband (Proceedings)*, Karlsruhe, SO-5.002, p 231. https://www.dgg-2014.de/downloads/DGG_Tagungsband.pdf. Accessed 19 Sept 2024
- The ObsPy Development Team (2020) ObsPy Tutorial Release 1.2.0. <https://docs.obspy.org>. Accessed 19 Sept 2024
- Trnkoczy A, Bormann P, Hanka W, Holcomb LG, Nigbor RL, Shinohara M, Shiobara H, Suyehiro K (2012) Site Selection, Preparation and Installation of Seismic Stations. In: Bormann P. (ed.), *New Manual of Seismological Observatory Practice 2 (NMSOP-2)*, Potsdam, Deutsches

- GeoForschungsZentrum GFZ, 1–139. https://doi.org/10.2312/GFZ.NMSOP-2_ch7
- Wassermann J (2012) Volcano Seismology. In: Bormann P (ed.), *New Manual of Seismological Observatory Practice 2 (NMSOP-2)*, Potsdam, Deutsches GeoForschungsZentrum GFZ 1–77. https://doi.org/10.2312/GFZ.NMSOP-2_ch13
- Weber K (2012) Erdbeben in der Eifel und dem Neuwieder Becken. In: Viereck L (ed) *Einblicke - vom Gestern zum Heute, 25 Jahre DVG, Mendig*, pp 84–94
- Wessel P, Luis JF, Uieda L, Scharroo R, Wobbe F, Smith WHF, Tian D (2019) The generic mapping tools version 6. *Geochem Geophys Geosyst* 20:5556–5564. <https://doi.org/10.1029/2019GC008515>
- Witt-Eickschen G, Kaminsky W, Kramm U, Harte B (1998) The nature of young vein metasomatism in the Lithosphere of the West Eifel (Germany): Geochemical and Isotopic Constraints from composite mantle xenoliths from the Meerfelder Maar. *J Petrology* 39:155–185. <https://doi.org/10.1093/ptro/39.1.155>
- Witt-Eickschen G (2007) Thermal and geochemical evolution of the shallow subcontinental lithospheric mantle beneath the Eifel: constraints from mantle xenoliths, a review. In: Ritter JRR, Christensen UR (eds) *Mantle Plumes*. Springer, Berlin, pp 323–337. https://link.springer.com/chapter/10.1007/978-3-540-68046-8_9
- Yavuz E, Sertçelik F, Livaoğlu H, Woith H, Lühr B-G (2019) Discrimination of quarry blasts from tectonic events in the Armutlu Peninsula, Turkey. *J Seismol* 23:59–76. <https://doi.org/10.1007/s10950-018-9793-2>

Publisher's Note Springer Nature remains neutral with regard to jurisdictional claims in published maps and institutional affiliations.